International Journal of Multiphase Flow 137 (2021) 103548

Contents lists available at ScienceDirect

International Journal of Multiphase Flow

journal homepage: www.elsevier.com/locate/ijmulflow

Breakup and coalescence of large and small bubbles in sudden expansions and contractions in vertical pipes

G.E.O. Celis [b], C.M.P. Rosero [b], J.B.R. Loureiro [a,b,*], A.P. Silva Freire [a,b]

[a] Interdisciplinary Center for Fluid Dynamics (NIDF/UFRJ), R. Moniz Aragão 360, 21941-594, Rio de Janeiro, Brazil
[b] Mechanical Engineering Program (PEM/COPPE/UFRJ), C.P. 68503, 21941-972, Rio de Janeiro, Brazil

ARTICLE INFO

Article history:
Received 29 March 2020
Revised 1 December 2020
Accepted 15 December 2020
Available online 17 December 2020

Keywords:
Multiphase flow
Bubble breakup
Bubble coalescence
Pipe expansion
Pipe contraction

ABSTRACT

The present work studies the dynamics of large and small bubbles in sudden expansions and contractions in vertical pipes. The experimental apparatus was designed to permit changes in flow patterns through singularities provoked by an expansion followed by a contraction. The data were obtained through particle image velocimetry and the shadow sizer technique. Size and velocity distributions for small and long bubbles are presented for six vertical pipe positions and compared with existing theories for the motion of small and large confined bubbles. Results for the mean velocity profiles, local shear rate and turbulent kinetic energy of the continuous phase are also presented. Predictions on the permissible largest diameter of bubbles as a function of space coordinates and flow conditions based on phenomenological theories are compared with the experimental data. Results indicate that bubble breakup and coalescence are essentially ruled by the dynamic pressure forces of the turbulent motions, but shear induced breakup is also observed for the small and large bubbles. The formation of a gas pocket in the contraction is identified as an important promoter of bubble breakup.

1. Introduction

The assemblage of virtually every piping system is only made possible through the use of multiple connecting parts. The occurrence of junctions, bends, valves, enlargements and reductions is the rule rather than the exception in industry.

The practical consequence is that flows in common applications are extremely complex, with the appearance of large regions of separated flow, secondary structures, streamline deflections and intense turbulent fields. A further complication to many problems is the presence of two distinct phases. This is a most serious difficulty since inadequate information on the position of interfaces and the relative velocities of the component fluids severally hampers any systematic solution. In particular, the correct prediction of the statistical properties of two-phase flows downstream of singularities in pipes is a challenging pursuit, for it requires the understanding of the intricate relations between the turbulence of the continuous and dispersed phases, velocity gradients and interfacial and pressure forces.

The present work is concerned with the description of two-phase flows in sudden expansions and contractions in vertical pipes. The incoming flow patterns are bubble and slug flows, and the emphasis is on the quantitative characterization of the breakup and coalescence mechanisms of small and large bubbles. The phenomenology of problem is to be discussed elsewhere. In the experiments, an expansion is followed by a contraction with the same aspect ratio and six positions are considered for the assessment of the flow statistics (Fig. 1). The pipe diameters are 19 and 44 mm. The measuring techniques are Particle Image Velocimetry (PIV) and Shadow Sizing (SS). Measured quantities include the size and velocity distributions of small and large bubbles, the mean velocity and turbulent kinetic energy of the liquid phase and pressure changes. The experimental conditions are such as to promote bubble or slug flows throughout the whole vertical column or a flow pattern transition from slug (upstream of the expansion) to bubble (in the region between the expansion and the contraction), returning to slug flow downstream of the contraction. Fig. 1 illustrates the experimental setup and three different experimental conditions for a constant liquid flow rate ($Q_l = 1.24\ m^3h^{-1}$) where bubble-to-bubble-to-bubble (gas flow rate $Q_g = 0.12\ m^3h^{-1}$), slug-to-bubble-to-slug ($Q_g = 0.27\ m^3h^{-1}$) and slug-to-slug-to-slug flows ($Q_g = 0.69\ m^3h^{-1}$) are observed.

The work does not study the behavior of a small number of bubbles created under controlled conditions, but rather complex flows with a large number of bubbles that freely interact with each

* Corresponding author.
E-mail address: jbrloureiro@mecanica.coppe.ufrj.br (J.B.R. Loureiro).

https://doi.org/10.1016/j.ijmultiphaseflow.2020.103548
0301-9322/

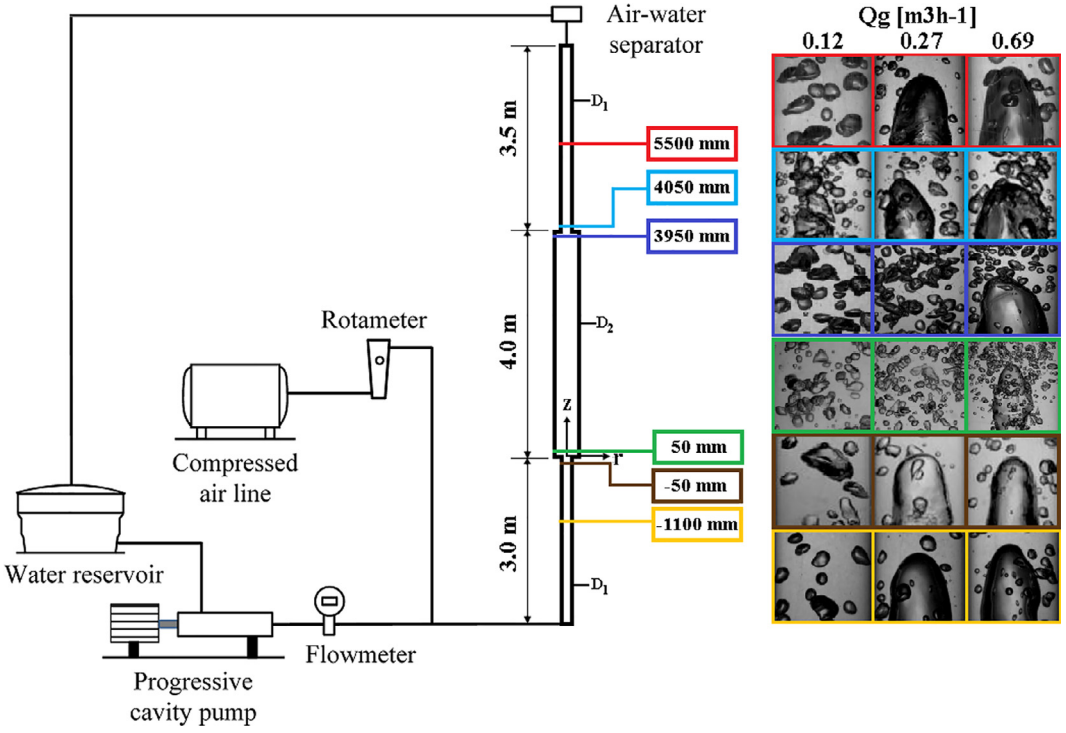

Fig. 1. Overview of the vertical pipe and the measurement positions. $Q_l = 1.24$ m^{3}h^{-1}; $Q_g = 0.12, 0.27, 0.69$ m^{3}h^{-1}. Location of the coordinate system.

other. Thus, every conceivable type of bubble breakup and coalescence was observed in the experiments.

In the expansion, it has been observed that small bubbles break mainly due to violent turbulent dynamic pressure forces. Large bubbles break due to interfacial instabilities in the entrance region and the high level of turbulence in the central region of the pipe. In the transition from slug to bubbly flow, coalescence was observed as a result of collisions provoked by turbulence, buoyancy and wake effects.

In the contraction, both the breakup and coalescence processes are strongly dependent on the appearance of a *vena contracta*. In bubbly flow, small bubbles tend to agglomerate at the contraction, yielding a gas ring pocket that is stable. Downstream of the gas pocket, small bubbles are stretched and fragmented in the near wall region. Upon the action of a large bubble (slug flow), the gas pocket is displaced downstream and eventually coalesce with the bulk of the large bubble as it passes through the smaller diameter pipe. In the initiation phase of the formation of a new gas pocket, small bubbles coalesce yielding a moderate size bubble that detaches from the wall and generates a wake that provokes further coalescence. The next formed gas pocket remains stable until it is hit by a large bubble and the process is repeated periodically.

The work thus shows that large and small bubbles that move across expansions and contractions break and coalesce due to a variety of mechanisms: shear forces, turbulent fluctuations, interface instabilities, wake and buoyant effects.

The next section presents a short discussion on the evolution of bubble size distributions and gas-liquid flows in expansions and contractions. Section 3 introduces the experimental setup, the measurement techniques (PIV and SS) and the flow conditions. Section 4 introduces the distributions of bubble diameter and velocity, profiles of shear rate and turbulent kinetic energy, mean velocity of the continuous phase and pressure profiles. Section 5 concludes the work. Fundamental theories on the dynamics of rising bubbles are presented in the appendix.

2. Short literature review

2.1. The evolution of bubble size distributions

A great difficulty in proposing models for the evolution of bubble size distributions is to express breakup and coalescence rates in terms of the basic properties of the related fluids and the flow dynamics. Of course, an essential element to the advancement of models is knowledge on bubble breakup frequency and daughter size distribution, collision frequency and efficiency.

The fundamental processes that lead to bubble breakup and coalescence may in some cases be interrelated, very often implying a difficult observation of the experiments and interpretation of the data. For instance, in very agitated systems, with a large concentration of bubbles, breakup and coalescence are observed to occur simultaneously. Clearly, turbulence plays a dual role since it provokes on bubbles the impact of eddies (breakup) or other bubbles (coalescence). In view of these difficulties, the tendency in literature has been on the development of simplified experiments where physical effects can be easily isolated and modeled. This methodology has clearly permitted great advances on physical modeling, but struggles to furnish generalized models capable of furnishing good predictions when combined effects are present.

In literature, models are thus built on the notion that breakup results from interactions of the dispersed bubbles with the continuous phase and coalescence results from bubble interactions with the continuous phase and themselves. Furthermore, the distinction between the physical mechanisms that lead to bubble breakup and coalescence has naturally instigated authors to address both problems separately in the literature. Most works discuss isolated aspects of either problem from simplifying hypotheses and particular data sets. Model generalizations are limited by the diversity of complex effects induced through geometry and flow conditions.

For example, the review article of Lasheras et al. (2002) on bubble breakup only considers systems in which the dispersed and

continuous phases posses the same mean velocity, and turbulence can be considered homogeneous and isotropic. The review article of Liao and Lucas (2009) discusses models for breakup frequency based on four physical effects: turbulent fluctuation and collision, viscous shear stress, shearing-off and surface instability. The distribution of daughter bubble size is described from the stand point of empirical, phenomenological and statistical models. Liao and Lucas (2009) state that breakup results from a competition between the turbulent stresses of the continuous phase, which tend to disintegrate the bubble, and the combined effects of the surface stress and the viscous stress of the bubble, which tend to restore its shape.

Liao and Lucas (2010), in another review article, discuss bubble coalescence. In all cases, collision and contact are the major mechanisms for bubble coalescence. Collision is considered to occur as a result of motion induced by turbulent fluctuations in the continuous phase, capture by turbulent eddies, shear flow, distinct bubble rise velocities and wake interactions. Since not all collisions result in bubble coalescence, expressions are introduced to account for coalescence efficiency. Liao and Lucas (2010) list three models for prediction of bubble coalescence efficiency: film drainage, energetic collisions and critical approach velocity.

In the present work, all the above physical effects are discussed in connection with two-phase flows in expansions and contractions. The chief mechanism for bubble breakup and coalescence in the present study is, however, turbulent agitation.

2.2. Gas-liquid flows in expansions and contractions

Most of the previous studies on the effects of pipe expansions and contractions on flow properties strive to develop models for the prediction of local pressure differences and changes in the velocity and void fraction profiles (Schmidt and Friedel, 1997; Attou and Bolle, 1999; Ahmed et al., 2007; 2008). The mechanics of bubble breakup and coalescence is rarely addressed.

The experimental work of Rinne and Loth (1996) investigates bubble flow across a sudden expansion in a vertical pipe. The emphasis of the study is on the prediction of local interfacial area concentration based on local measurements of bubble velocity and size distributions. Rinne and Loth (1996), however, do not specifically discuss the breakup and coalescence of bubbles.

Bubbly flows were also investigated by Aloui et al. (1999) in a horizontal pipe. In this work, the authors attribute to the increase in the dynamic pressure across the expansion the observed decrease of 20% in bubble diameter.

Ahmed et al. (2008) observed the changes in flow pattern for a horizontal air-oil pipe flow across a sudden expansion. Depending on the void fraction of the incoming flow a variety of downstream flow patterns were observed. Typically, intermittent flow may keep its pattern or transition to elongated bubbles or stratified/wavy flow; annular mist flow can keep its original pattern or transition to stratified wavy flow. The authors remarked that the phase redistribution suffers a strong effect of the upstream flow pattern and the area ratio of the expansion.

The work of Galinat et al. (2005) discusses the breakup of drops downstream of a concentric orifice fitted to a pipe. The work concludes that the mean drop diameter downstream of the restriction changes with the inverse of the square root of the pressure drop. The study identifies different breakup mechanisms and presents data on the breakup probability, the mean number of fragments and the daughter drop distribution.

Azzopardi et al. (2014) studied slug flow across a 76/38 mm sudden contraction. Their results support the idea that the fluid structures are essentially stretched as they pass into the smaller diameter pipe. Basically, the passage frequency of slugs is conserved, whereas the sizes and velocities increase.

3. Experiments

The experimental apparatus consists of three aligned segments of transparent vertical pipe with respective lengths of 3.0, 4.0 and 3.5 m. The first and third segments have an internal diameter of $D_1 = 19$ mm, the intermediate segment has a diameter of $D_2 = 44$ mm. The resulting expansion and contraction sections are illustrated in Fig 1. Please note the origin of the coordinate system, located at beginning of the expansion.

The test section is supplied with water and gas through a "T" junction located at the bottom of the vertical pipe. The T-junction is connected to the discharge line of a progressive cavity pump and to an air compressor. The water flow rate was measured through a calibrated electromagnetic flow meter (overall uncertainty of 1% of the reading). The gas flow rate was obtained from readings of a calibrated rotameter (3% overall uncertainty of the full scale). Pressure was measured through a Rosemount 3051 pressure transmitter. On the top of the column a gas-liquid gravitational separator was installed. The separated air was directly released to the atmosphere, whereas the water flow was returned to the reservoir.

The flow conditions are shown in Table 1. The specified liquid and gas flow rates permit successive flow pattern changes at the expansion and contraction as previously shown in Fig. 1. Though the images in Fig. 1 are not under the same magnification, they depict the characteristic gas-liquid phase distribution in each region of the vertical pipe.

The changes in flow configuration are further illustrated through the flow pattern map of Taitel et al. (1980) (Fig. 2) for pipes with 25 and 50 mm ID (the present experiments were performed in 19 and 44 mm ID pipes). Fig. 2 shows that the green symbols are well within the region of bubble flow, so that the singularities are bound to impose a bubble/bubble/bubble flow configuration. The blue symbols on the other hand, are very close to the transition region for slug flow. The experiments have shown that under these conditions the observed configuration was slug/slug/slug (Fig. 1). The intermediate conditions shown through the red symbols are the conditions that allowed the establishment of a slug/bubble/slug configuration. Under the red dot condition, slug flow was observed in the inlet and outlet 25 mm pipes. This pattern changed to bubble flow as the flow area was expanded to a 1:5.36 ratio.

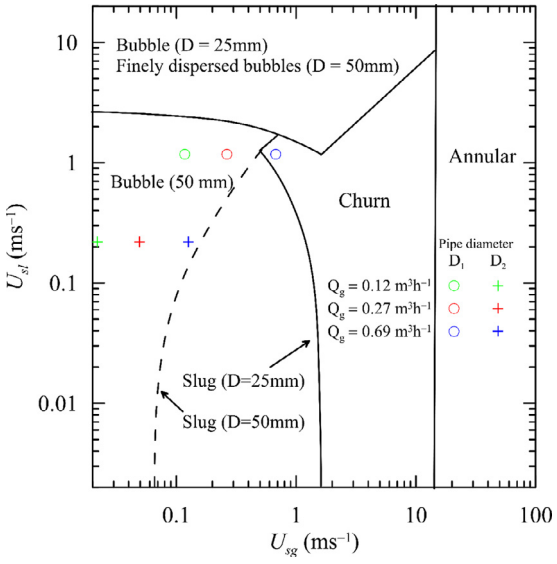

Fig. 2. Flow pattern map (Taitel et al. (1980)) for the experimental conditions.

Table 1
Flow experimental conditions, where D_1 (= 19 mm) is the diameter of inlet and outlet segments, D_2 (= 44 mm) is the diameter of the intermediate segment, Q_l and Q_g are the volumetric liquid and gas flow rates in m^3h^{-1}, $U_{sl_{D_1}}$, $U_{sl_{D_2}}$, $U_{sg_{D_1}}$ and $U_{sg_{D_2}}$ are the superficial liquid and gas velocities at the inlet and intermediate segments, respectively.

Flow pattern($D_1/D_2/D_1$)	$Q_l(m^3h^{-1})$	$Q_g(m^3h^{-1})$	$U_{sl_{D_1}}(ms^{-1})$	$U_{sl_{D_2}}(ms^{-1})$	$U_{sg_{D_1}}(ms^{-1})$	$U_{sg_{D_2}}(ms^{-1})$
Bubble/Bubble/Bubble	1.24	0.12	1.22	0.23	0.12	0.02
Slug/Bubble/Slug	1.24	0.27	1.22	0.23	0.26	0.05
Slug/Slug/Slug	1.24	0.69	1.22	0.23	0.68	0.13

In the present investigation, two sets of measurements were performed. Initially, high speed shadow sizer technique was used to characterize the breakup and coalesce phenomena and to quantify the properties of the discrete gas phase. Next, the velocity of the continuous liquid phase was measured through a 15 Hz 2D Particle Image Velocimetry system. In all measurements the test sections were enclosed by an acrylic rectangular box filled with water to minimize optical distortions due to pipe curvature.

The Shadow Sizer (SS) system from Dantec Dynamics™ was composed by two constellation led systems and by a 12 bit Speed Sense M310 camera, with 1,280 x 800 pixel resolution and maximum acquisition rate of 3,260 frames per second. The two led systems were placed behind a diffuser installed at the back of the transparent box to provide uniform background illumination. The camera was placed on the opposite side of the box, in front of the two led sources, and was equipped with a 60 mm Micro Nikkor lens f/2.8D. The opening of the lens diaphragm and the exposure time were adjusted to provide the largest depth of field around the pipe certerline, so as to keep most of the gas bubbles into focus. The linear horizontal dimension of the field of view of the camera was adjusted for the larger pipe as to slightly exceeds the diameter of the intermediate pipe (see Fig. 1). In general, the field of view ranged from 53.8(H)x172.0(V) mm to 70.8(H)x226.6(V) mm. The led systems had a controllable emission time and were triggered according to the acquisition frame rate adjusted for the camera, which was 1,400 frames per second for most of the experimental conditions. The camera was operated in single frame mode and the system synchronization was controlled by the software Dynamic Studio (version 2015a).

The images acquired through the Shadow Sizer system were processed by a dedicated contour detection algorithm implemented in MATLAB. A sequence of image processing operations, including subtraction of the mean background were applied to sharpen the contour of bubbles, so that edge detection could be accurately performed. Once a closed contour was determined, the position of the bubble centroid, i.e. the geometric center of the plane figure, given by the arithmetic mean position of all the points in the contour, was calculated. The mean equivalent diameter of small bubbles is defined as the diameter of a spherical particle having the same surface as the one measured by the detected contour. For long bubbles, the length is defined as the distance between the top pixel on the bubble nose contour and the bottom pixel on the bubble tail. The reconstruction method described in Matamoros et al. (2014) was used for bubbles bigger than the height of the field of view. For the present measurements, the spatial resolution ranged between 9.48 to 17.7 m/px, depending on the measurement station. The velocity of discrete particles was evaluated using a correlation similarity criterion to match a pair of bubbles. After the corresponding images of a same bubble in two consecutive frames were identified, the velocity was determined with sub-pixel accuracy. The estimated overall uncertainties of bubble size and velocity with a confidence interval of 90% are expressed as error bars in Figs. 20 and 21.

The bubble size and velocity distributions presented in Section 4, which are expressed at a given measurement station (axial position z), were actually obtained in a centered window of width D_p (= local pipe diameter) and height 50 mm. This height was chosen to permit that for any given frame a representative number of bubbles was considered in the statistics (the mean diameter of the small bubbles was normally below 4 mm). Only bubbles that were entirely visible in the windows were considered in the statistics. To make sure that diameter and velocity results were uncorrelated and that only different bubbles were considered in the statistics, a time lapse of 100 Δt to 500 Δt (Δt = 1/1,400) was considered between pictures, depending on the flow conditions. For the statistics of the large bubbles, all bubbles were considered individually (no bubbles were discarded). To obtain the statistics of the small and long bubbles, over 800 and 300 data were considered respectively. Fig. 3 shows typically considered images for the statistics of the flow in the expansion and contraction.

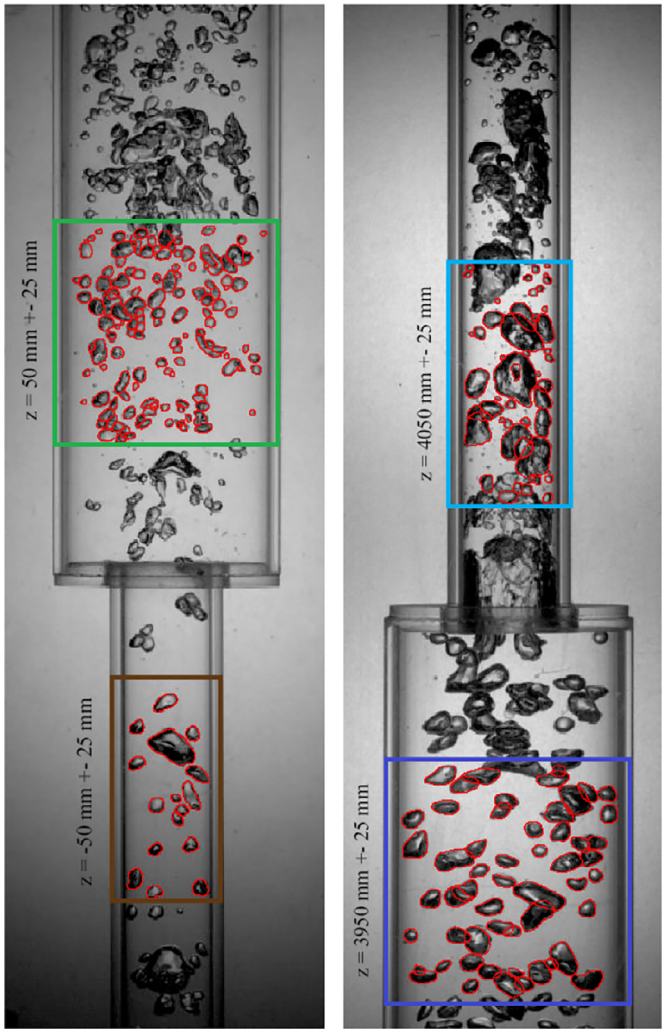

Fig. 3. Identification of small bubbles for the calculation of size and velocity distributions at the expansion and contraction.

Mean velocity and turbulent statistics of the continuous phase were measured through Particle Image Velocimetry (PIV). The 2D PIV system used the same camera previously described together with a Litron Nd-Yag laser of 135 mJ and 15 Hz repetition rate. A vertical laser lightsheet was generated by a series of spherical and cylindrical lens at the pipe centerline. The laser sheet thickness was about 1 mm at the test sections. To minimize intense optical reflections from the surfaces of bubbles, nearly neutrally buoyant fluorescent Rhodamine painted polystyrene particles (ρ = 1.05 gcm^{-3}), 20 m size, were used as tracers. These seeding particles, when illuminated by the Nd-Yag laser (532 nm wavelength), emit light in the yellow-orange region of the spectrum (572 to 594 nm). To avoid the glares from the bubble surface, the camera was fitted with a narrow-band 570 nm optical filter, so that just the fluorescent radiation from tracer particles is captured. As suggested by Nogueira et al. (2003), with the purpose of improving the resolution and accuracy of the liquid velocity estimate near the bubble surface, the led illumination system was used simultaneously to the PIV measurements. To enhance the contrast of the bubble shape, the led systems were covered by a red transparent film and fired simultaneously to the laser source. The led systems were kept at the same position, in front of the camera, promoting an uniform background illumination in the red-orange wavelength. This procedure allows the acquisition of images that discriminate equally well the fluorescent seeding particles and the position of the bubbles contour. This set up permitted the calculation of the velocity field in the liquid film and in the flow around the dispersed bubbles. The software Dynamic Studio (version 2015a) was used for system synchronization, image acquisition and processing. The camera was triggered in double frame mode. Typically 2,000 image pairs have been acquired for the velocity characterization.

Before the PIV evaluation routines can be applied to the acquired images, they must undergo some pre-processing steps to create a mask that can remove the disperse flow phase. This masking process is based on a sequence of arithmetic and morphology operations, since the images are still gray scale. The first morphological operation is erosion, where the value of the output pixel is the minimum value of all pixels in the neighbourhood. This operation removes small objects – the seeding particles – so that only the substantive objects remains (the bubbles). Mean background subtraction is then performed to enhance the contrast between the bubbles and their background. The next step is to binarize the image to obtain the contour of the bubbles and finally, a filling operation is needed since some bubbles may present inner open areas due to non-uniform illumination or reflections. The images of the raw sequence are then masked. This procedure removes information from the dispersed phase, allowing the calculation of the velocity field only in the liquid film and around the dispersed bubbles.

The continuous velocity field was evaluated through the software Dynamic Studio of Dantec Dynamics (version 2015a). The adaptive correlation routine was used to iteratively optimize the size and shape of each interrogation area to local flow gradients and seeding densities. All the interrogation areas that showed interference with the masks were excluded from the velocity estimates. Different time delays between the laser pulses were selected and adjusted to the velocity magnitudes expected in each section of the pipe. The spatial resolution of the PIV measurements was 0.3x0.3 mm; this value was achieved through a series of subsequent analysis using interrogation areas varying from 32x32 to 8x8 pixels, with a grid step size reduction of 2x2 pixels. The signal-to-noise ratio was close to 4.

Similar PIV measurements have been performed for slug flows by van Hout et al. (2002) and Shermer et al. (2007) and for bubble flows by Ziegenhein and Lucas (2016) and Hessenkemper and Ziegenhein (2018). In particular, Ziegenhein and Lucas (2016) discusses adequate methods to overcome the sampling bias in PIV measurements of bubble flows. If the flow contains enough particles and the velocity is calculated at a specific point, a windowed ensemble average over time provides reasonable results and should be used. This ensemble averaging procedure was used in the present work.

Table 2
Water properties at 25 °C.

Property	Mean	Standard deviation
Surface tension (N.m^{-1})	0.063131	3.83E-06
Dynamic viscosity (Pa.s)	0.0009	1.96E-05
Density (kg.m^{-3})	996.04	0.121

The physical properties of water at 25 °C were determined through a Krüss K100 tensiometer (*Wilhelmy* plate method), a MCR 302 rheometer (conical plate geometry, shear rate ($\dot{\gamma}$) ramp from 100 to 1000 s^{-1}) and a DMA 502 densimeter. Three measurements were conducted under the same conditions for the determination of the average value of every property. The data are shown in Table 2.

4. Experimental results

The phenomenology of bubble breakup and coalescence in expansions and contractions with a detailed graphical illustration of the involved processes will be discussed elsewhere. A short discussion of the phenomena, however, is in order here.

In the expansion, most bubble breakup and coalescence occurred due to turbulent effects. Collision provoked by the different rise velocity of bubbles, wake effects and turbulent agitation often result in bubble coalescence, in a process that is often followed by immediate bubble breakup. The breakup process is very complex and often a bubble is split into multiple parts. Bubble breakup is the net result of bubble interaction in the expansion. Bubble breakup due to shearing effects was also noted.. Most observed breakups due to shearing effects were binary, but some splittings resulted in three bubbles. In addition to the center region of the pipe, small bubbles were observed to coalesce in the recirculating flow region.

In a vertical contraction, one typical and extremely important aspect of bubble breakup and coalescence is the formation of a gas pocket. The gas pocket (or gas ring) is observed for incoming bubbly or slug flows and plays the key role in the formation of a *vena contracta* with a complex unsteady behavior. In fact, depending on the incoming bubble conditions (size, spatial organization, velocities) the gas pocket can be stable or unstable.

The following data on bubble size distributions and mean velocity are compared with fundamental results related to the rising velocity of bubbles and their splitting and coalescence. The expressions to which the results are compared with are presented in an appendix for the sake of paper readability.

4.1. Bubble size distributions

The equivalent diameter distributions for the small bubbles followed a log-normal behavior; the large bubbles distributions followed a Gaussian behavior. To improve legibility of the results, the figures show only the adjusted distributions to the corresponding histograms, where f corresponds to the probability density function. Discussions on fitted distributions to bubble diameters can be found in Lage and Esposito (1999) and Gonçalves et al. (2018). Two typical bubble histograms are shown in Fig. 4 with their respective fitted log-normal distributions.

For the small and large bubbles, the size distributions across the sudden expansion and contraction at positions z = - 1,100, - 50, 50,

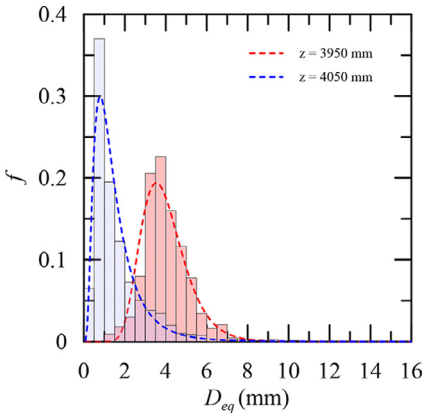

Fig. 4. Typical bubble equivalent diameter histograms with respective fitted log-normal distributions. Q_l = 1.24 m^3h^{-1}, Q_g = 0.12 m^3h^{-1}.

3,950, 4,050 and 5,500 mm are shown in Figs. 5 and 6. The main statistics for the sizes of small and long bubbles are also shown in Tables 3 and 4 respectively.

For the lowest gas flow rate, Q_g = 0.12 m^3h^{-1}, long bubbles were not observed. The equivalent diameter distributions of the small dispersed bubbles upstream of the expansion at positions z = -1,100 and - 50 mm are seen to almost coincide ($D_{eq_{mean}} \approx$ 3.2 mm; Fig. 5a). Following the expansion, a large reduction in mean diameter is observed, of about 24% ($D_{eq_{mean}} \approx$ 2.4 mm), as a result of the dominant bubble breakup process. The coalescence of bubbles over the long vertical 44 mm ID pipe (4 m) provokes a considerable increase in mean diameter, to $D_{eq_{mean}} \approx$ 4.0 mm. The breakup process at the contraction with the important presence of the gas pocket yields a distribution with very small bubbles and $D_{eq_{mean}} \approx$ 1.6 mm (a reduction of 60%). Far downstream

Table 3
Small bubbles diameter statistics (mm). Q_l=1.24 m^3h^{-1}. s is the standard deviation.

Q_g (m^3 h^{-1})		0.12	0.27	0.69
z=–1,100 mm	$D_{eq_{min}}$	0.91	1.09	1.06
	$D_{eq_{max}}$	10.32	6.68	7.35
	$D_{eq_{mean}}$	3.21	2.61	2.47
	s	1.31	0.92	1.13
z=–50 mm	$D_{eq_{min}}$	1.49	0.94	0.62
	$D_{eq_{max}}$	9.27	11.62	3.94
	$D_{eq_{mean}}$	3.14	2.70	1.70
	s	1.30	1.16	0.57
z=50 mm	$D_{eq_{min}}$	0.64	0.76	0.50
	$D_{eq_{max}}$	8.38	10.48	3.98
	$D_{eq_{mean}}$	2.40	2.50	1.38
	s	1.23	1.32	0.56
z=3,950 mm	$D_{eq_{min}}$	1.53	1.39	0.79
	$D_{eq_{max}}$	7.68	7.87	6.96
	$D_{eq_{mean}}$	3.96	3.88	3.02
	s	1.05	1.39	1.15
z=4,050 mm	$D_{eq_{min}}$	0.36	0.54	0.49
	$D_{eq_{max}}$	10.28	11.18	7.63
	$D_{eq_{mean}}$	1.58	1.96	1.69
	s	1.28	1.30	0.92
z=5,500 mm	$D_{eq_{min}}$	1.61	1.38	1.39
	$D_{eq_{max}}$	6.43	10.36	13.31
	$D_{eq_{mean}}$	3.97	3.39	3.64
	s	1.1	1.72	2.29

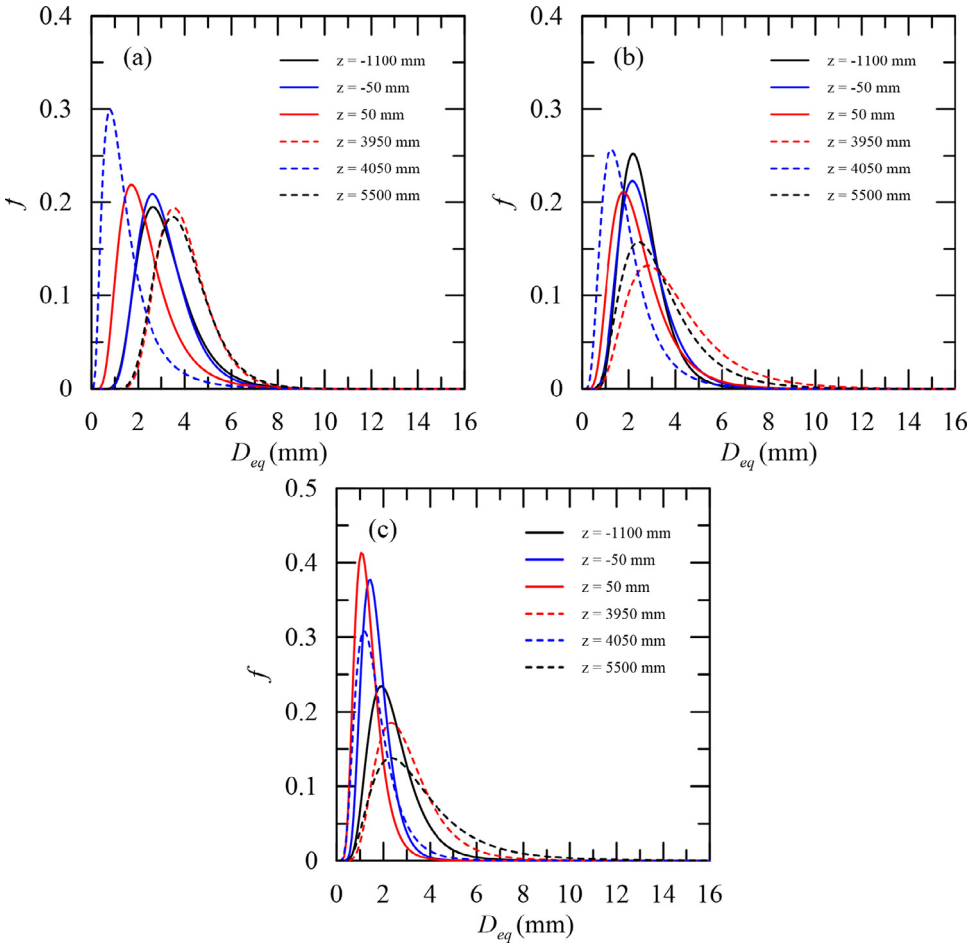

Fig. 5. Equivalent diameter distributions of the small bubbles for Q_l = 1.24 m^3h^{-1} and: a) Q_g = 0.12 m^3h^{-1}, b) Q_g = 0.27 m^3h^{-1}, c) Q_g = 0.69 m^3h^{-1}.

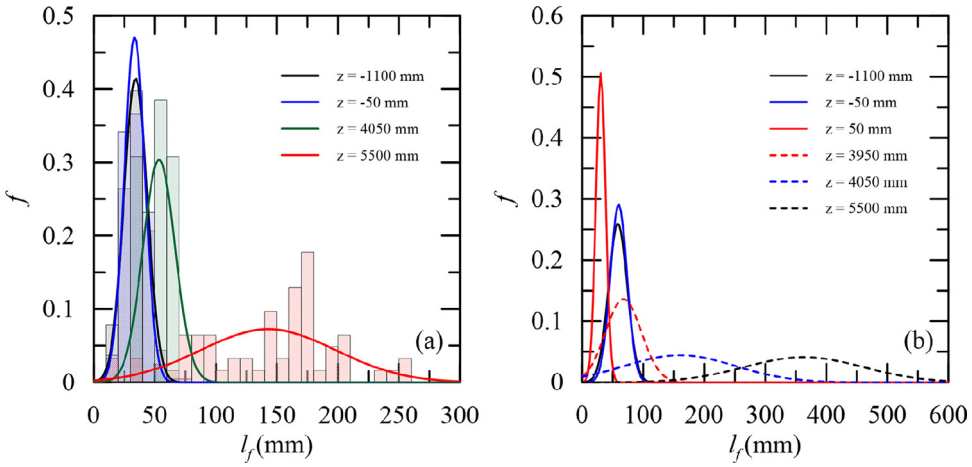

Fig. 6. Size distributions of the long bubbles for Q_l = 1.24 m^{3}h^{-1} and: a) Q_g = 0.27 m^{3}h^{-1}, b) Q_g = 0.69 m^{3}h^{-1}.

of the contraction (z = 5,500 mm), the bubble distribution returns to the level encountered just before the contraction with $D_{eq_{mean}} \approx$ 4.0 mm (again as a result of bubble coalescence in a long stretch of pipe).

The results for the moderate gas flow rate (Q_g = 0.27 m^{3}h^{-1}, Fig. 5b) are similar to those just described above. However, for this flow condition, long bubbles were observed in the two 19 mm pipes (before the expansion and after the contraction). The diameter distributions for the small bubbles for the first two measurement locations were very alike ($D_{eq_{mean}} \approx$ 2.7 mm). The expansion produces a decrease (of 7%) on the size of the small bubbles, followed by an increase (of 55%) in the 4 m long, 44 mm ID pipe. The breakup of bubbles at the contraction was significant; $D_{eq_{mean}}$ was reduced in 50%. At position z = 5,500 mm, the increase in $D_{eq_{mean}}$ was of 73%.

Regarding the long bubbles, for Q_g = 0.27 m^{3}h^{-1} (Fig. 6), the bubble length (l_f) distributions at positions z = - 1,100 and -50 mm coincide with $l_{f_{mean}}$ about 34 mm. Downstream of the contraction, long bubbles with $l_{f_{mean}} \approx$ 54 mm are recorded; far downstream of the contraction, $l_{f_{mean}} \approx$ 143 mm.

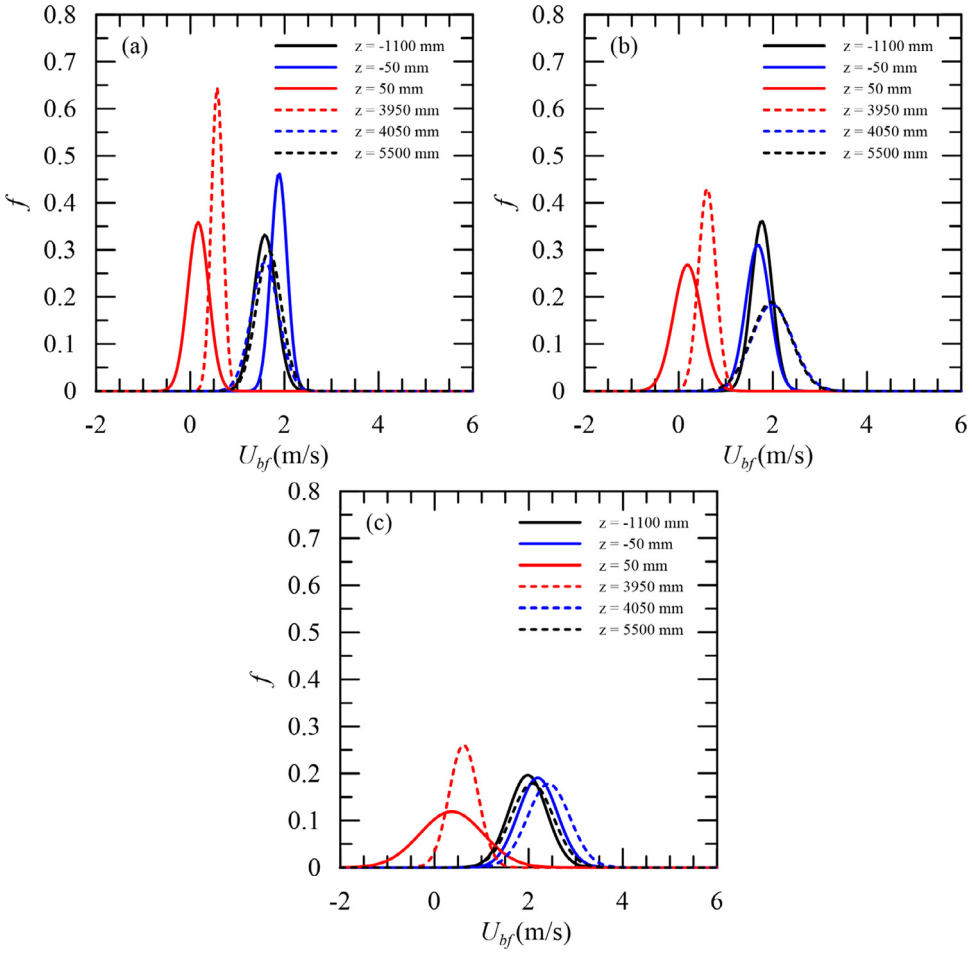

Fig. 7. Small bubbles velocity distributions at different stations for Q_l = 1.24 m^{3}h^{-1} and: a) Q_g = 0.12 m^{3}h^{-1}, b) Q_g = 0.27 m^{3}h^{-1}, c) Q_g = 0.69 m^{3}h^{-1}.

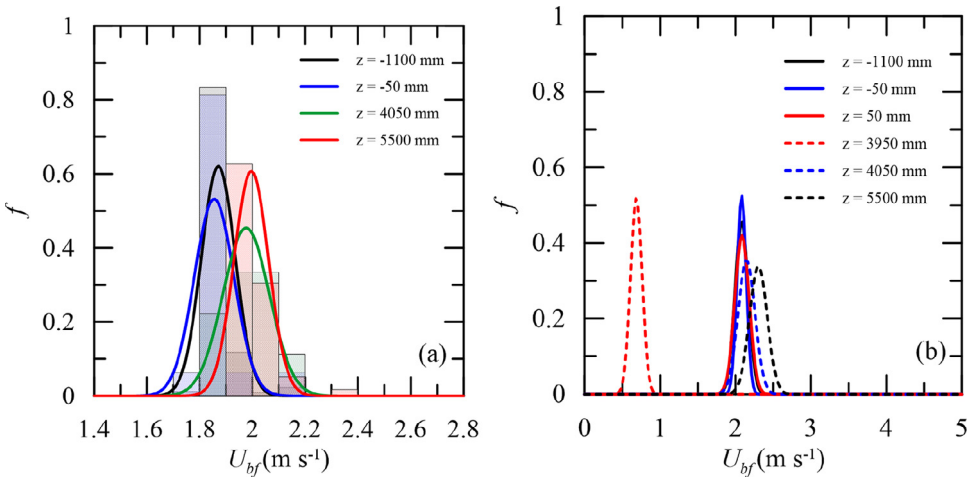

Fig. 8. Large bubbles velocity distributions at different stations for Q_l = 1.24 m^{3}h^{-1} and: a) Q_g = 0.27 m^{3}h^{-1}, b) Q_g = 0.69 m^{3}h^{-1}.

Only for the highest gas flow rate (Q_g = 0.69 m^{3}h^{-1}), long bubbles were observed to survive throughout the pipe length (including the singularities provoked by the expansion and contraction). For the small bubbles (Table 3), the equivalent diameter statistics for position z = - 50 mm shows a mean diameter decrease in relation to position z = - 1,100 mm ($D_{eq_{mean}}$ is reduced from 2.5 to 1.7 mm). The presence of very long bubbles enhanced the coalescence of small bubbles into the long bubble. This coalescence mechanism is simple and has been observed before. Small bubbles of sizes comparable to the thickness of the film that surrounds the long bubble are squashed and coalesce onto the long bubble. The result is a decrease in the mean value of D_{eq} with a corresponding increase in the mean value of l_f (Table 4). At the expansion, the reduction in $D_{eq_{mean}}$ is of 19%. Shortly before and after the contraction, $D_{eq_{mean}}$ respectively increases to 3.02 mm and decreases to 1.69 mm. At position z = 5,500 mm, the mean equivalent diameter is 3.64 mm. Fig. 6 shows that the long bubbles exhibit a very similar length distribution for positions z = - 1,100 and - 50 mm. After the expansion, $l_{f_{mean}}$ is reduced in 50%. In the following positions, $l_{f_{mean}}$ assume the values 65.43 (z = 3,950 mm), 158.05 (z = 4,050 mm) and 373.72 (z = 5,500 mm) mm. To put this into a different perspective, at positions z = - 50, 3,950 and 5,500 mm the bubble lengths correspond to 3.15D_p, 3.59D_p and 19.67D_p. These results confirm the very well known fact that one of the simplest ways to produce very long bubbles in a short pipe length is to use a contraction.

4.2. Bubble velocity distributions

The statistics of the rise velocities of the small bubbles are shown in Fig. 7 and Table 5. In Table 5, the theoretical predictions were obtained with the mean equivalent diameter data of Table 3. To account for the confinement effects, the bubbles were considered *fluid spheres*, that is, Eq. (A.15) was used. The flowing stream effects were incorporated through Eq. (A.19) with C_0 = 1.2 (the preferred value of Wallis (1969)).

For all gas flow rates, the velocity distributions at stations z = - 1,100, - 50, 4050 and 5,500 mm (19 mm pipe) are very close. Small differences are observed due to the existing extra development lengths or the presence of large bubbles, but, in general, the distributions are very close. In the 44 mm ID pipe, the velocity distributions at position z = 50 and 3,950 mm show clear distinct shapes. The reduction in mixture velocity and the very agitated flow at the expansion provoke a sharp decrease in mean velocity with a large

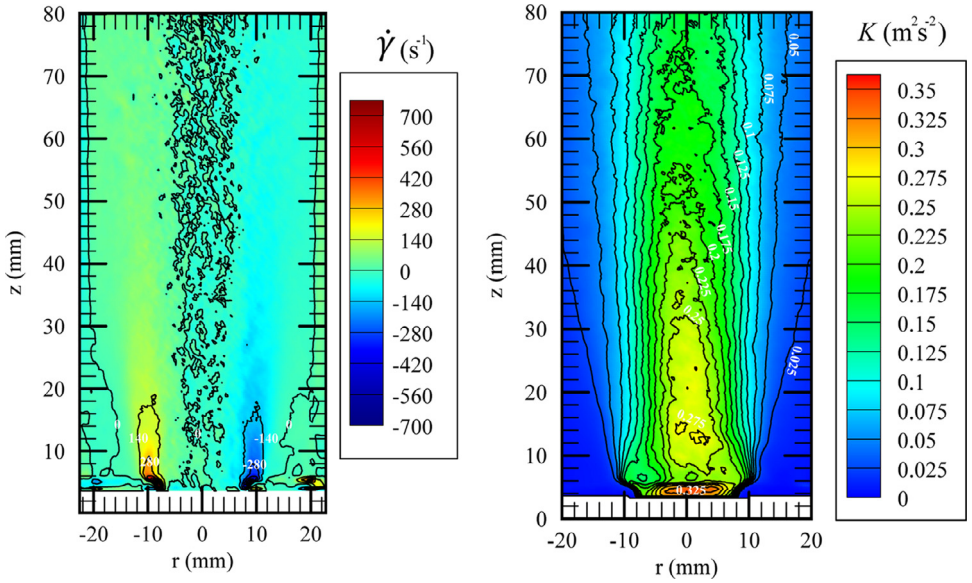

Fig. 9. Shear rate (s^{-1})(left) and turbulent kinetic energy per unit mass (m^{2}s^{-2})(right) in the expansion; Q_l = 1.24 m^{3}h^{-1} and Q_g = 0.69 m^{3}h^{-1}.

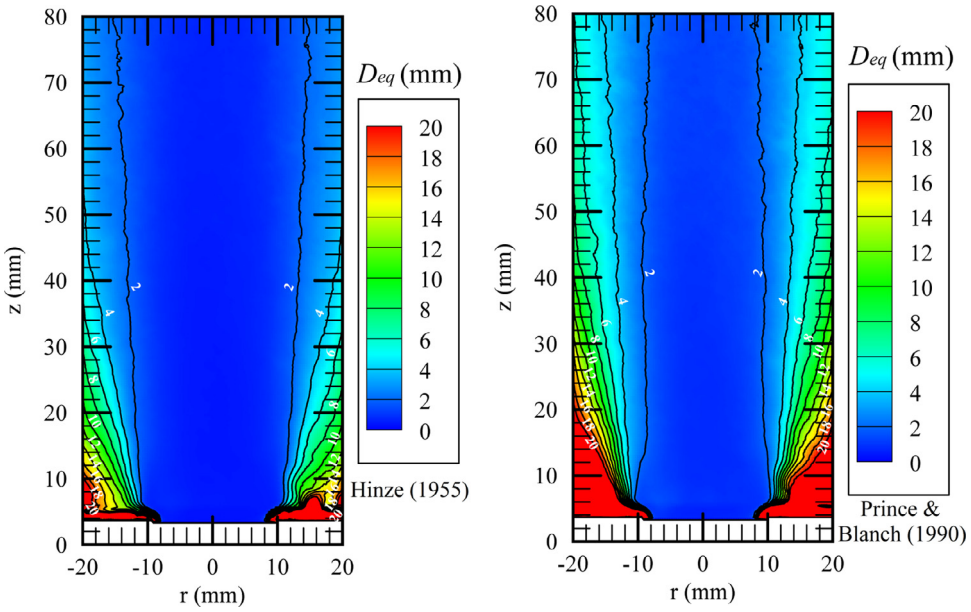

Fig. 10. Maps of the maximum bubble equivalent diameter according to the critical We of Hinze (1955) (left) and Prince and Blanch (1990) (right) for the expansion. Q_l = 1.24 m^3h^{-1} and Q_g = 0.69 m^3h^{-1}.

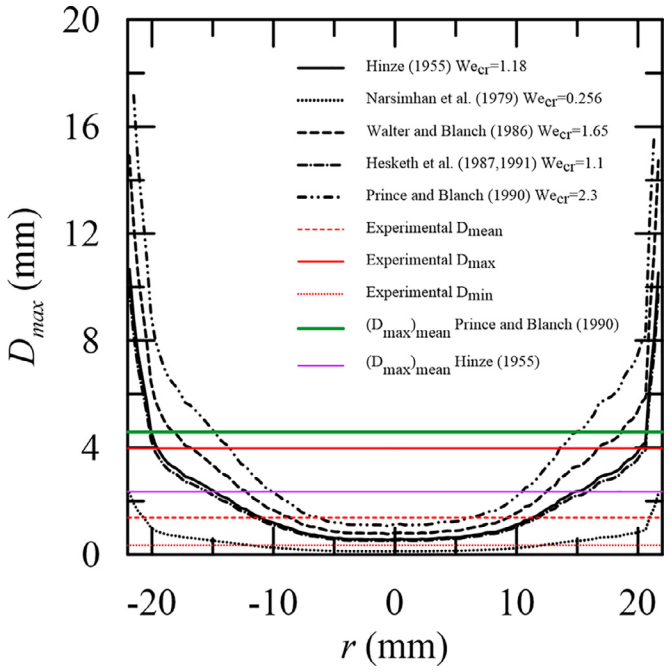

Fig. 11. Prediction of the maximum bubble equivalent diameter at z = 50 mm. Q_l = 1.24 m^3h^{-1} and Q_g = 0.69 m^3h^{-1}.

Table 4
Long bubbles length statistics (mm). Q_l=1.24 m^3h^{-1}. s is the standard deviation.

	Q_g (m^3h^{-1})	0.27	0.69
z = −1,100 mm	$l_{f_{min}}$	13.7	17.9
	$l_{f_{max}}$	73.92	111.42
	$l_{f_{mean}}$	34.23	58.40
	s	9.42	14.98
z = −50 mm	$l_{f_{min}}$	16.17	21.13
	$l_{f_{max}}$	55.12	84.05
	$l_{f_{mean}}$	33.39	59.97
	s	8.05	12.60
z = 50 mm	$l_{f_{min}}$		18.90
	$l_{f_{max}}$		46.75
	$l_{f_{mean}}$		30.28
	s		7.61
z = 3,950 mm	$l_{f_{min}}$		35.71
	$l_{f_{max}}$		122.75
	$l_{f_{mean}}$		65.43
	s		26.57
z = 4,050 mm	$l_{f_{min}}$	33.50	34.00
	$l_{f_{max}}$	69.83	313.77
	$l_{f_{mean}}$	53.76	158.05
	s	12.55	83.49
z = 5,500 mm	$l_{f_{min}}$	13.20	142.36
	$l_{f_{max}}$	255.90	613.38
	$l_{f_{mean}}$	143.16	373.72
	s	52.21	99.80

variance. In the long 44 mm pipe, the small bubbles accelerate to a much higher value of U_{bf}, close to the values theoretically predicted by the equations shown in the appendix (Table 5); the variance at z = 3,950 mm for all flow conditions was observed to be smaller than that at z = 50 mm.

The velocity distributions correspond to the whole set of small bubbles, they have not been discriminated according to bubble diameters. For this reason, the predictions shown in Table 5 must be seen as very good. In general, the theory tends to overpredict the present mean velocities of small bubbles by 10%.

For the long bubbles, the distributions of U_{bf} are presented in Fig. 8 and Table 6. For the lowest gas flow rate, at positions z = - 1,100 and - 50 mm, the flow is not yet completely developed so that the measured velocities are about 4% below the expected value. Following the contraction, the velocities of the large bubbles that pass through positions z = 4,050 and 5,500 mm are respectively 1.99 and 2.00 ms^{-1}, about 3.6% above the expected value of 1.93 ms^{-1}. The large bubble formation processes suggest that the flow configuration here is such that the bubble velocity is affected by the length of the short liquid slugs ahead of it. A detailed discussion on the influence of slug length on bubble velocity can be found in Fagundes Netto et al. (2019).

For Q_g = 0.69 m^3h^{-1}, the long bubble velocity distributions are almost coincident at positions z = - 1,100, - 50 and 50 mm. The large bubbles keep their velocities as they penetrate the expansion up to z = 60 mm; the observed velocities were 14% below the ex-

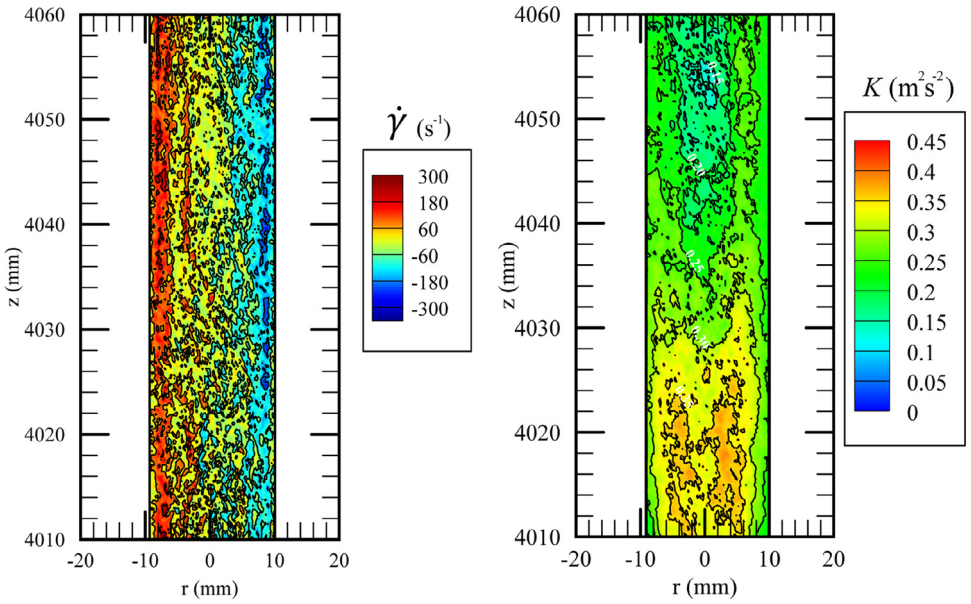

Fig. 12. Shear rate (s^{-1})(left) and turbulent kinetic energy per unit mass (m^2s^{-2})(right) in the contraction; $Q_l = 1.24\ m^3h^{-1}$ and $Q_g = 0.69\ m^3h^{-1}$.

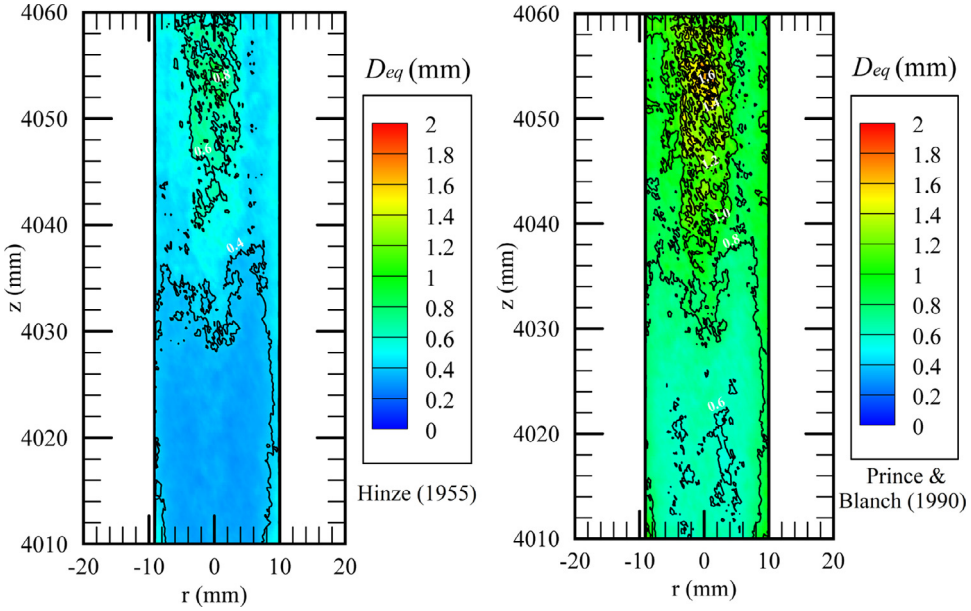

Fig. 13. Maps of the maximum bubble equivalent diameter according to the critical W_e of Hinze (1955) (left) and Prince and Blanch (1990) (right) for the contraction. $Q_l = 1.24\ m^3h^{-1}$ and $Q_g = 0.69\ m^3h^{-1}$.

pected fully developed value. The reduction in bubble velocity in the larger ID pipe is observed at position $z = 3{,}950$ mm. The measured velocity at this position was 5.7% over the expected value for a fully developed flow. Following the contraction, U_{bf} is noted to return to the expected value for a 19 mm ID pipe ($= 2.42\ ms^{-1}$).

4.3. Shear rate, turbulent kinetic energy and maximum predicted bubble diameter

The contours of shear rate ($\dot{\gamma}$) and turbulent kinetic energy per unit mass (K) in the expansion are shown in Fig. 9 for the slug flow pattern ($Q_l = 1.24\ m^3h^{-1}$, $Q_g = 0.69\ m^3h^{-1}$). It is clear from Fig. 9 that the layers of high shear rates that bound the recirculating fluid regions promote bubble breakup (up to $z = 30$ mm). Most bubble splittings, however, occur in regions of very high K, over $0.25\ m^2s^{-2}$.

To evaluate K in Eq. (A.24), isotropy was considered in the plane orthogonal to z, that is, $\text{ord}(\sqrt{u_x'^2}) = \text{ord}(\sqrt{u_y'^2})$, so that $2K = u_z'^2 + 2u_x'^2$. $\dot{\gamma}$ was evaluated through a first order central finite difference discretization scheme for each component.

The data displayed in Fig. 9 can be applied directly to Eq. (A.24) to yield a map of the permissible maximum bubble diameter. Since the results of Fig. 10 resort to the local values of K, the generally preferred locations for bubble splitting are well represented, in particular, with the use of the $W_{e_{crit}}$ of Prince and Blanch (1990) ($= 2.3$). Fig. 10, however, only furnishes a qualitative view of the phenomenon. A quantitative comparison with the present measurements is carried out in Fig. 11, where the radial $D_{\max}$ profile for $z = 50$ mm is presented. In the central region of the pipe, the predicted $D_{\max}$ for all considered $W_{e_{crit}}$ is much lower than the actual observed $D_{\max}$. The averaged value

Table 5
Rise velocity of small bubbles. *Exp.* refers to experiments; *Theor.* to theoretical predictions according to the equations shown in the Appendix A. The particularly used equation is a function of the considered $D_{eq_{mean}}$.

z (mm)	Exp. Mean U_{bf} (ms^{-1})	Theor. U_{bf} (ms^{-1})
	$Q_g = 0.12$ (m^3 h^{-1})	
−1100	1.60	1.79
−50	1.88	1.79
50	0.38	0.54
3,950	0.61	0.50
4,050	1.59	1.87
5,500	1.67	1.77
	$Q_g = 0.27$ (m^3 h^{-1})	
−1,100	1.76	1.98
−50	1.66	1.98
50	0.25	0.57
3,950	0.66	0.54
4,050	2.01	2.02
5,500	1.96	1.96
	$Q_g = 0.69$ (m^3 h^{-1})	
−1,100	2.20	2.48
−50	2.19	2.52
50	0.64	0.73
3,950	0.62	0.64
4,050	2.42	2.53
5,500	2.24	2.45

Table 6
Rise velocity of long bubbles. *Exp.* refers to experiments; *Theor.* to the theoretical results of the appendix based on Eq. (A.20).

z (mm)	Exp. Mean U_{bf} (ms^{-1})	Theor. U_{bf} (ms^{-1})
	$Q_g = 0.27$ (m^3 h^{-1})	
−1,100	1.87	1.93
−50	1.85	1.93
50		0.56
3,950		0.56
4,050	1.99	1.93
5,500	2.00	1.93
	$Q_g = 0.69$ (m^3 h^{-1})	
−1,100	2.08	2.42
−50	2.09	2.42
50	2.09	0.65
3,950	0.69	0.65
4,050	2.16	2.42
5,500	2.30	2.42

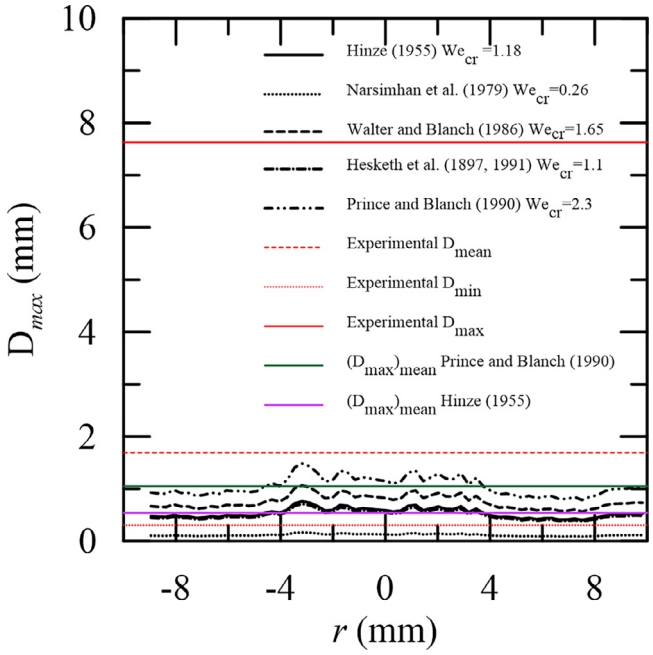

Fig. 14. Prediction of the maximum bubble equivalent diameter at $z = 4{,}050$ mm. $Q_l = 1.24$ m^{3}h^{-1} and $Q_g = 0.69$ m^{3}h^{-1}.

of $D_{\max}$ (with $We_{crit} = 2.3$) is, however, very close to the averaged measured $D_{\max}$.

The contours of $\dot{\gamma}$ and K for the contraction are shown in Fig. 12 for $Q_l = 1.24$ m^{3}h^{-1} and $Q_g = 0.69$ m^{3}h^{-1}. The regions of high $\dot{\gamma}$ are located close to wall, where some bubble splitting was observed to occur. In the central region of the pipe, the bubble breakup results from the very high levels of K, over 0.35 m^{2}s^{-2}. A map of $D_{\max}$ is shown in Fig. 13, according to the We_{crit} of Hinze (1955) and Prince and Blanch (1990). Contrary to the maps for the expansion ($z = 50$ mm), the results for the contraction are not very useful. This is partially due to the existence of the gas pocket, which adds much complication to the breakup and coalescence processes and whose effects cannot be captured by the simple arguments developed in the appendix. The awkwardness of the arguments is emphasized by Fig. 14, where the radial $D_{\max}$ profiles for $z = 4{,}050$ mm are shown. The averaged value of $D_{\max}$ furnished

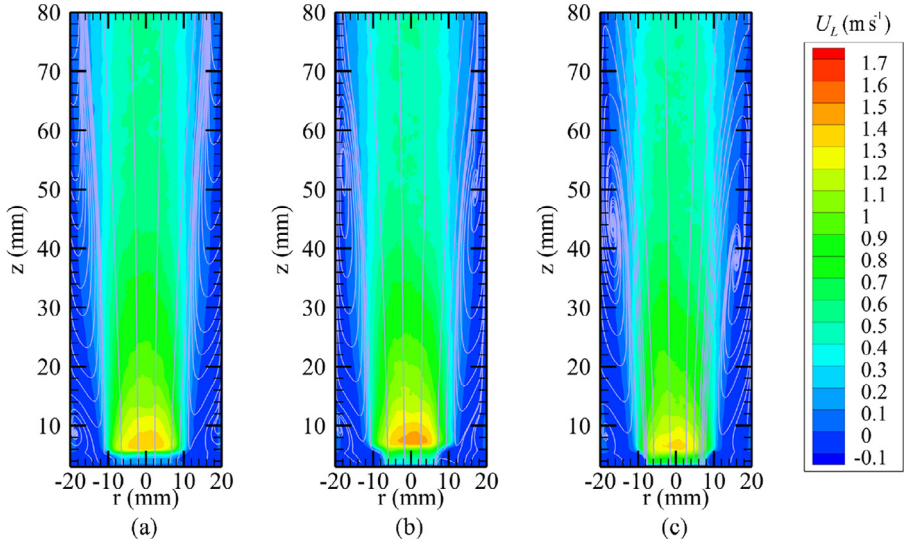

Fig. 15. Streamlines and mean liquid velocity distribution map in the expansion for $Q_l = 1.24$ m^{3}h^{-1} and: a) $Q_g = 0.12$ m^{3}h^{-1}, b) $Q_g = 0.27$ m^{3}h^{-1}, c) $Q_g = 0.69$ m^{3}h^{-1}.

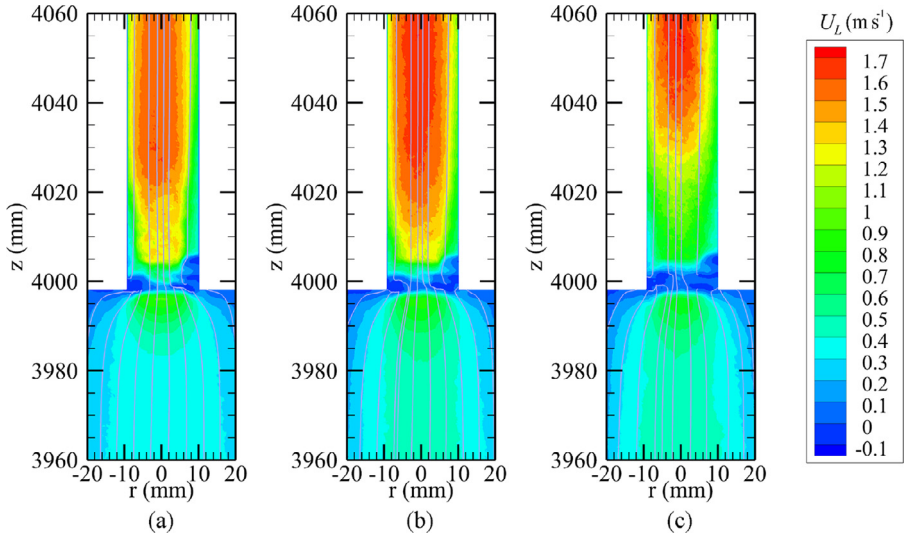

Fig. 16. Streamlines and mean liquid velocity distribution map in the contraction for Q_l = 1.24 m^{3}h^{-1} and: a) Q_g = 0.12 m^{3}h^{-1}, b) Q_g = 0.27 m^{3}h^{-1}, c) Q_g = 0.69 m^{3}h^{-1}.

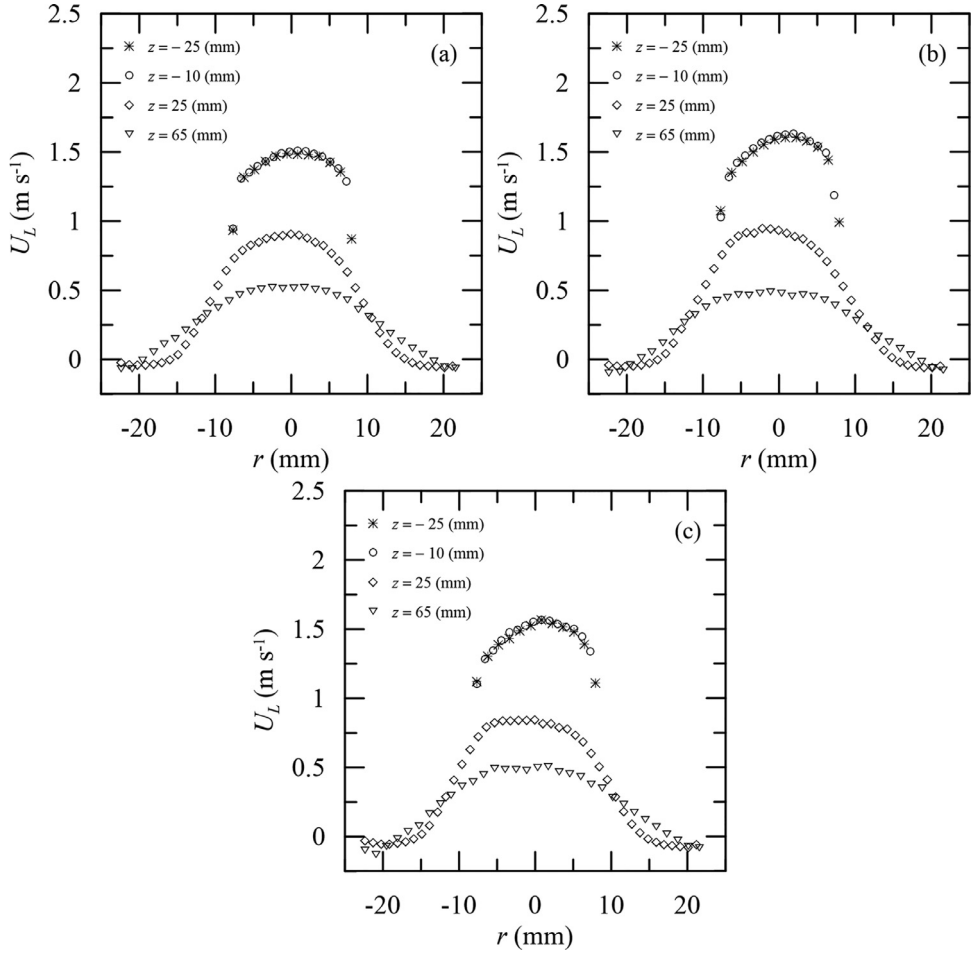

Fig. 17. Mean liquid velocity profiles through the expansion for Q_l = 1.24 m^{3}h^{-1} and: a) Q_g = 0.12 m^{3}h^{-1}, b) Q_g = 0.27 m^{3}h^{-1}, c) Q_g = 0.69 m^{3}h^{-1}.

by the theories is 1.05 mm, a value well below the experimental D_{max} (= 7.6 mm).

4.4. Mean velocity of the continuous phase and pressure profiles

For the sake of completeness some properties of the continuous phase are discussed next.

Streamlines and mean velocity distribution maps of the continuous phase in the expansion and contraction are shown respectively in Figs. 15 and 16. Two positions upstream and two positions downstream of the expansion and contraction are shown respectively in Figs. 17 and 18.

Fig. 17 shows that the flow upstream of the expansion is fully developed. The increase in gas flow rate increases the mean veloc-

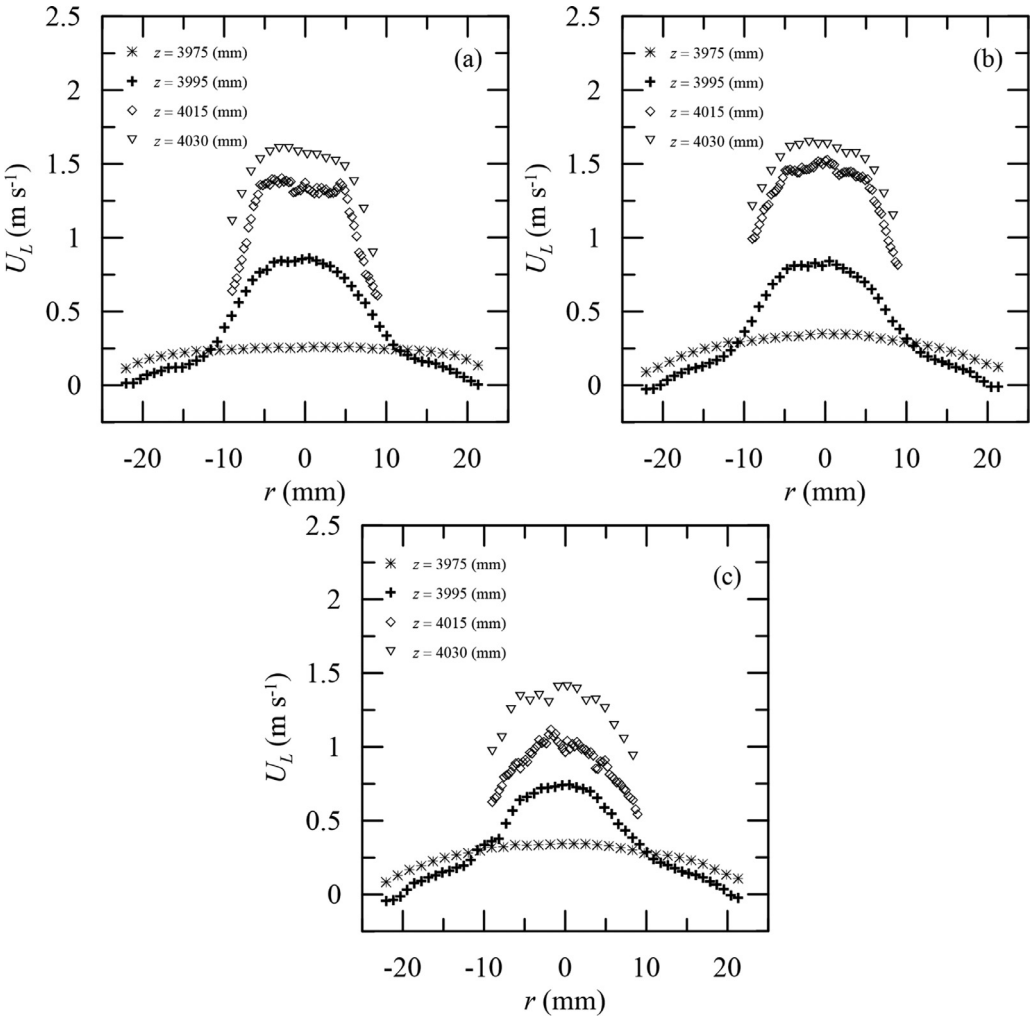

Fig. 18. Mean liquid velocity profiles through the contraction for Q_l = 1.24 m^{3}h^{-1} and: a) Q_g = 0.12 m^{3}h^{-1}, b) Q_g = 0.27 m^{3}h^{-1}, c) Q_g = 0.69 m^{3}h^{-1}.

ity in the centerline (as expected due to the passage of the large bubbles). Downstream of the expansion (z = 25 mm), the negative velocities of the recirculation region are clearly noted, along with the high shear region and high velocities near the center portion of the pipe.

Fig. 18 shows the mean velocity profiles as the flow approaches the contraction. Upstream of the restriction, the velocity distribution shows a fully developed profile that is progressively deformed into a high velocity region near the pipe centerline, with small negative values at the tails corresponding to the flow recirculation region. A general overview of this behaviour is shown if Figs. 16a-c, where the dark blue regions around z = 4,000 mm reveal the presence of recirculating flow and of the *vena contracta*. At positions z = 4,015 and 4,030 mm large distortions are observed in the mean velocity profiles as a result of the intense bubble activity (breakup and coalescence). Figs. 18a,b correspond to bubbly/bubbly and bubbly/slug flows, respectively. In Fig. 18a, at z = 4,015 mm, the mean velocity profile is irregular but relatively flat in its central region. In Fig. 18b (z = 4,015 mm), the shape of the profile tends to show a possible maximum, indicating the passage of larger bubbles. Despite the irregularity in the flow, this tendency is further evident in Fig. 18c (z = 4,015 mm), where U_L does not show any flat portion in the central region. Fig. 18c corresponds to the slug/slug flow condition where very long bubbles are observed in the central pipe. The characterization of the near wall velocity profiles was difficult at positions z = 4,015 and 4,030 mm due to presence of the gas ring and the resulting permanent detachment of small bubbles.

An integration of U_L over the cross sectional area of the pipes was carried out to verify mass conservation of the liquid phase. To all flow conditions the estimated Q_l from the local PIV measurements were mostly within 10% in error of the expected value. For Q_g = 0.12 m^{3}h^{-1}, the average error over the eight measurement positions (z = - 25, - 10, 25, 65, 3,975, 3,995, 4,015 and 4,030 mm) was 6.9%. For the two remaining conditions Q_g = 0.27 m^{3}h^{-1} and Q_g = 0.69 m^{3}h^{-1} the average errors were respectively 8.6 and 9.9%. The uncertainties in the measurement of the continuous phase stemmed from the natural difficulties in adequately resolving regions highly populated by bubbles, including the near wall region and regions of separated flow.

The changes in total pressure with coordinate z are shown in Fig. 19. The position of the 26 different pressure taps are shown in Fig. 19. In the expansion, the hydrostatic pressure was high enough to dominate the total pressure change across the singularity. The changes in pressure due to the reversible flow deceleration and the irreversible local losses were small. In the contraction the reversible changes are apparent. The single flow acceleration at the *vena contracta* locally lowers the pressure, which then continues to decrease due to the hydrostatic and irreversible components. For the two-phase flow, the local blockage effects provoked by the agglomeration of bubbles increases the local pressure which then starts to decrease again.

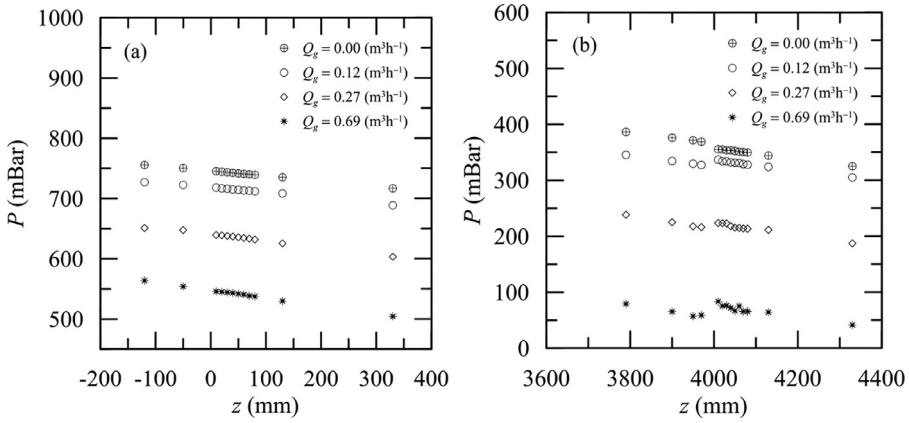

Fig. 19. Total pressure variation. a) expansion, b) contraction.

5. Final remarks

The present work identified and discussed the different types of mechanisms involved in bubble breakup and coalescence in sudden pipe expansions and contractions. The experimental apparatus was designed to permit changes in flow patterns through disturbances provoked by an expansion followed by a contraction in a vertical pipe.

The work has shown that large and small bubbles that move across expansions and contractions break and coalesce due to a variety of mechanisms: shear forces, turbulent fluctuations, interface instabilities, wake and buoyant effects. Predictions on the maximum bubble diameter by simple phenomenological theories provide reasonable results in the expansion. For the contraction, however, predictions are very poor. The formation of a gas pocket at the entrance of the contraction gives rise to a very complex bubble breakup process that cannot be easily captured by simple phenomenological arguments. Velocity distributions, on the other hand, are relatively well predicted by the existing theories.

In particular, the paper shows that for bubble and slug flows in vertical pipes, if a contraction is made to follow downstream of an expansion, the statistics for small bubble equivalent diameter far upstream of the expansion are different from those far downstream of the contraction.

The breakup and coalescence processes in both the expansion and contraction are, of course, much dependent on the flow patterns. Figs. 20(a,b) and 21(a,b) summarize the results for bubble sizes and rise velocities. The data cover small and large bubbles and show the maximum, mean and minimum values of the quantities.

In the expansion, located at 0 mm, breakup events are dominant for both the large and small bubbles; very little coalescence is observed. In the contraction (z = 4,000 mm), for the small bubbles, coalescence is observed but breakup is the prevalent occurrence. In fact, the bubble breakup process in the contraction for small bubbles is very strong. Large bubbles in the contraction, on the other hand, are essentially stretched as they penetrate into the smaller diameter pipe. Small bubbles suffer significant velocity changes along both the expansion and contraction (Fig. 20b), while the velocity of long bubbles changes considerably only in the contraction (Fig. 21b).

The work shows that in the expansion, small bubbles break mainly due to violent turbulent dynamic pressure forces. Large bubbles break due to interfacial instabilities in the entrance region and, also, the high level of turbulence in the central region of the pipe. In the slug-bubbly flow pattern transition, coalescence was observed as a result of turbulent and buoyant collisions and wake effects.

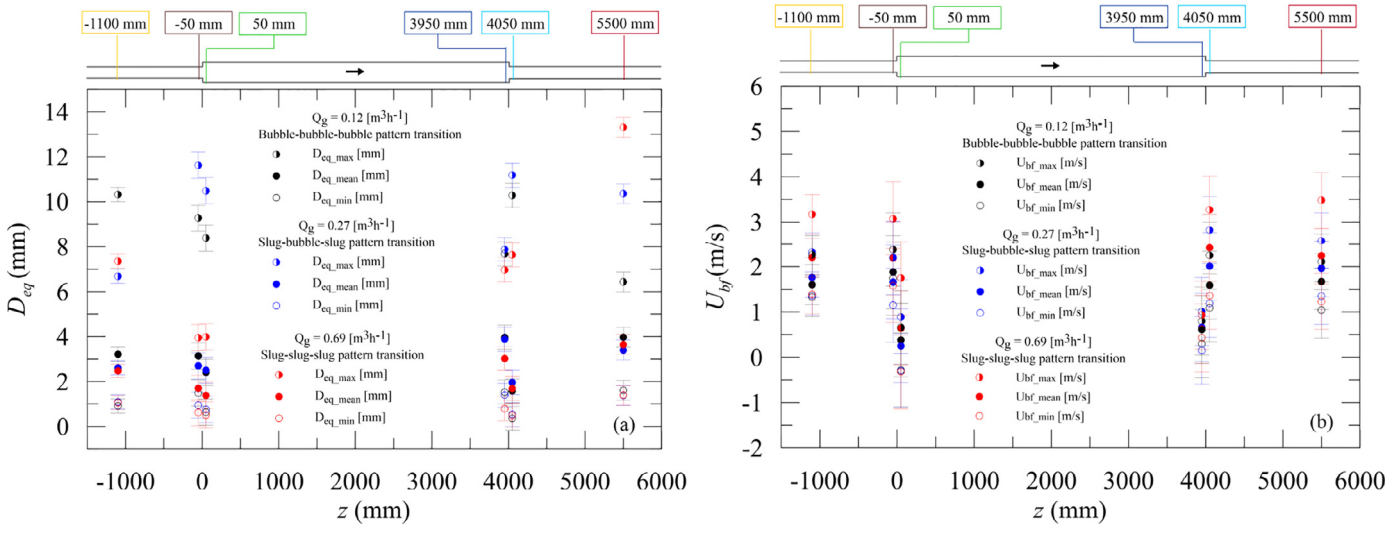

Fig. 20. Air-water flows through sudden expansions and contractions in vertical pipes: (a) equivalent diameter and (b) rise velocity of small bubbles.

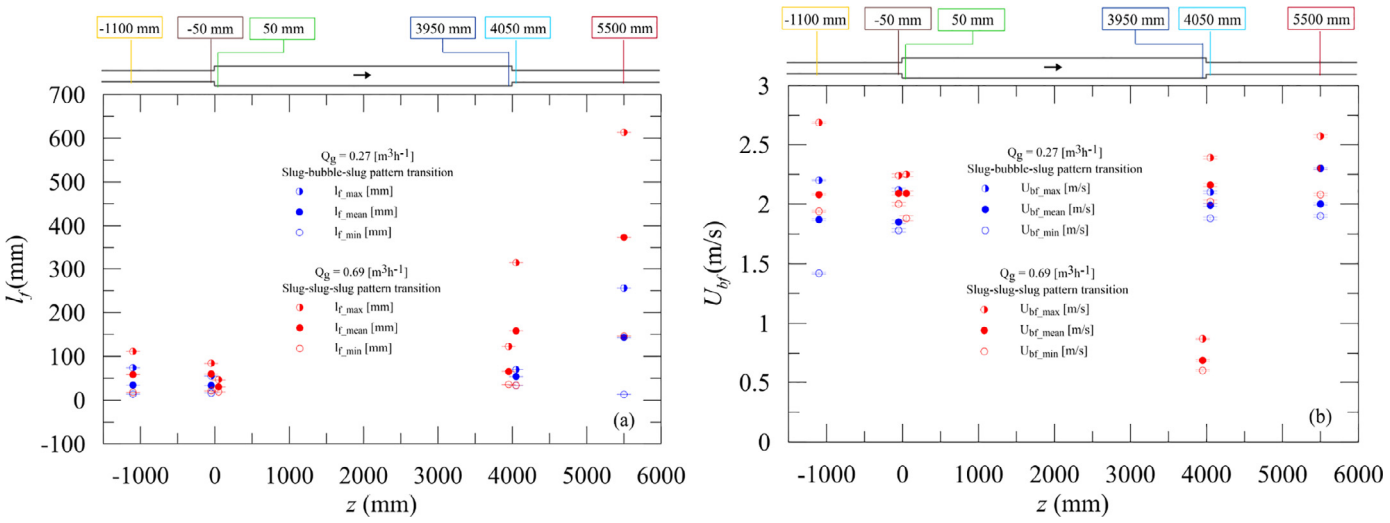

Fig. 21. Air-water flows through sudden expansions and contractions in vertical pipes: (a) length and (b) rise velocity of large bubbles.

In the contraction, both the breakup and coalescence processes are strongly dependent on the appearance of a *vena contracta*. In bubbly flow, small bubbles tend to agglomerate at the contraction, yielding a gas ring that is stable. Downstream of the gas pocket, small bubbles are stretched and fragmented in the near wall region. Upon the action of a large bubble (slug flow), the gas pocket is displaced downstream and eventually coalesce with the bulk of the large bubble as it passes through the smaller diameter pipe. In the initiation phase of the formation of a new gas pocket, small bubbles coalesce yielding a moderate size bubble that detaches from the wall and generates a wake that provokes further coalescence. The next formed gas pocket remains stable until it is hit by a large bubble and the process is repeated periodically.

Declaration of Competing Interest

The authors declare that they have no known competing financial interests or personal relationships that could have appeared to influence the work reported in this paper.

CRediT authorship contribution statement

G.E.O. Celis: Investigation, Validation, Methodology, Formal analysis. **C.M.P. Rosero:** Investigation, Validation, Methodology, Formal analysis, Data curation, Visualization. **J.B.R. Loureiro:** Methodology, Writing - review & editing, Project administration, Resources. **A.P. Silva Freire:** Conceptualization, Validation, Writing - original draft, Supervision.

Acknowledgements

APSF is grateful to the Brazilian National Research Council (CNPq) for the award of a Research Fellowship (No 307232/2019-0). JBRL benefited from a CNPq Research Fellowship (Grant No 309455/2016-2) and from further financial support through Grant FAPERJ E-26/203.257/2016. The work has been financially supported by FAPERJ through grant E-26/010.001275/2016 (Pronex Núcleo de Excelência em Turbulência).

Appendix A. Bubble dynamics

The present section introduces a short review on some fundamental results related to the dynamics of rising bubbles in unconfined and confined environments. This is a complex theme that should ideally discuss the motion of bubbles under the effects of (i) the physical properties of the continuous and dispersed phases, (ii) Reynolds number Re, (iii) the formation, size and shape of bubbles, (iv) cleanliness and (v) interaction phenomena (including breakup and coalescence). Here, this large scope is limited to a discussion on the rising rates of bubbles in steady uniform flow conditions. Nonetheless, the presently introduced theories are extremely important for the interpretation of the data presented in this work and are summoned to validate the physical arguments and the qualitative results of Section 4.

Important results are presented in Clift et al. (1978), where an unified treatment of solid particles, liquid drops and bubbles is attempted. In particular, this work reviews many relevant results on the description of the motion of fluids and solid particles in systems in which particle-particle interactions can be considered negligible. The dynamics of single bubbles is introduced in detail in Wallis (1969, 1974). In both references, the formation and the rise velocity of single bubbles are discussed together with many diverse effects such as their sizes and shapes, containing walls, void fraction and oscillations. Bubbles moving in inhomogeneous flows at moderate to high Reynolds numbers are reviewed by Magnaudet and Eames (2000).

A1. The rise velocity of a single bubble in extended liquids

The terminal velocity of a single bubble depends basically on a balance between buoyancy and drag forces, that is to say on the properties of the related fluids, the flow past the bubble and the volume of the bubble. However, as just mentioned above, complications arise through the action of surface tension, which influences the bubble shape, and cleanliness, which influences the boundary condition at the interface. Very small bubbles are nearly perfect spheres due to the dominant effects of surface tension. Bubbles whose surfaces are free of impurities do not satisfy the no-slip velocity condition on the surface. Rather, the condition of zero shear stress must be considered, so that liquid slip at the surface is allowed. One may then refer to *solid* spheres (those where it can be assumed that the liquid velocity goes to zero at the surface) or *fluid* spheres (where velocity slip is allowed).

To determine the terminal rising velocity of a bubble (U_∞) through extended liquids, Wallis (1974) suggests to consider the following dimensionless forms of the bubble velocity and radius

(R_b),

$$U^* = U_\infty \left(\frac{\rho_l^2}{\mu_l g \Delta\rho} \right)^{1/3} = \frac{4}{3} \left(\frac{R_e}{C_D} \right)^{1/3}, \tag{A.1}$$

$$R^* = R_b \left(\frac{\rho_l g \Delta\rho}{\mu_l^2} \right)^{1/3} = \frac{3}{32} \left(C_D R_e^2 \right)^{1/3}, \tag{A.2}$$

where

$$R_e = \frac{\rho_l U_\infty D_b}{\mu_l}, \tag{A.3}$$

and ρ_l = liquid density, μ_l = liquid viscosity, $\Delta\rho = \rho_l - \rho_g$, ρ_g = gas density, g = gravity acceleration, D_b = bubble diameter, C_D = drag coefficient.

In Equations (A.1–A.2), once a relationship between R_e and C_D is known, U^* can be expressed in terms of R^*. For a *solid* sphere, Eqs. (A.1–A.2) encapsulate all the relevant information. To account for further relevant physical effects on *fluid* spheres, additional dimensionless numbers need to be considered.

The relative balance between inertia and surface tension effects can be introduced through the Weber number,

$$W_e = \frac{\rho_l U_\infty^2 D_b}{\sigma}, \tag{A.4}$$

where σ = interface tension.

The balance between gravitational and surface tension effects is correlated by the Eötvös number,

$$E_o = \frac{g(\Delta\rho) D_b^2}{\sigma}. \tag{A.5}$$

Some of the physical properties of a given two-fluid system can be conveniently arranged to yield a highly important dimensionless number, the Morton number. This number is a constant for a known two-fluid system and is defined as

$$M_o = \frac{g\mu_l^4(\Delta\rho)}{\rho_l^2 \sigma^3}. \tag{A.6}$$

For bubbles that rise or fall freely in an unbounded environment, Clift et al., 1978 introduce a correlation between R_e, E_o and M_o through a graphical representation (Fig. A.22). This figure provides a simple means to estimate the shapes of bubbles and

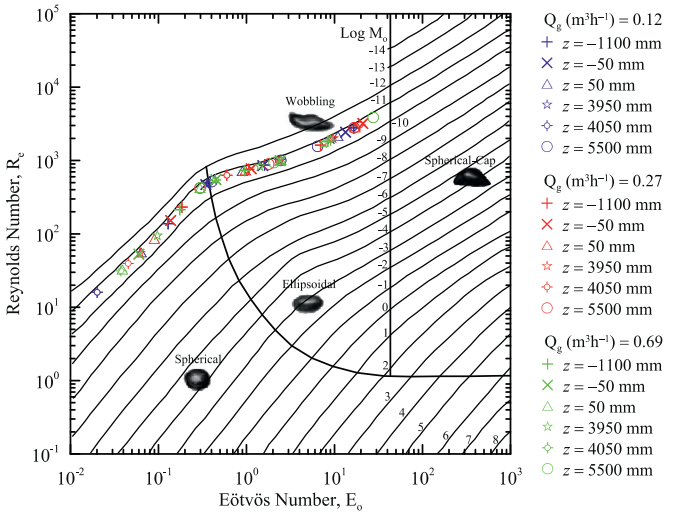

Fig. A.22. Shape and terminal velocity of bubbles and drops in an unbounded environment Clift et al. (1978). The symbols represent the range of E_o and M_o for the present experiments. Q_l = 1.24 m^3h^{-1}.

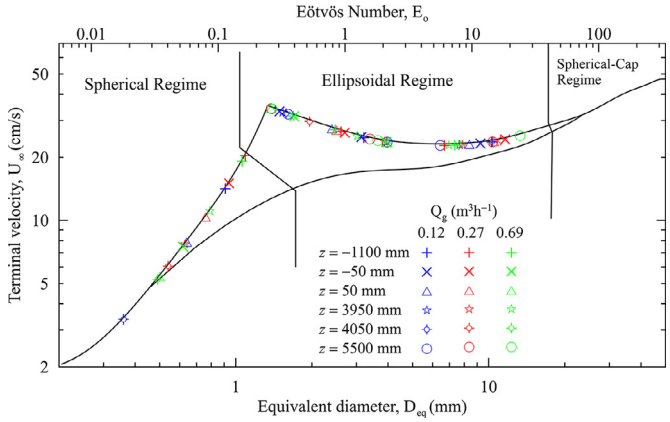

Fig. A.23. Terminal velocity of air bubbles in water (Clift et al., 1978). The symbols represent the range of E_o for the present experiments. Q_l = 1.24 m^3h^{-1}.

their terminal velocities for given E_o and M_o. Fig. A.22 approximately maps the principal shape regimes and subregimes (wobbling, skirted, dimpled ellipsoidal-cap) normally observed for bubbles. The terminal velocity follows directly from the estimated R_e. A notable aspect of Fig. A.22 is the large range of covered fluid properties and particle volumes. A similar but much more detailed shape regime map for bubbles in liquids can be found in Bhaga and Weber (1981).

The symbols shown in Fig. A.22 represent the range of E_o and M_o for the present experiments in terms of the bubble diameters (for the small bubbles) obtained for the several experimental conditions.

For the specific case of air bubbles in water, the terminal velocity is observed to depend strongly on surface contamination. The two curves shown in Fig. A.23 illustrate the large influence of surface-active contaminants on the rise velocity of bubbles in the ellipsoidal range; the curves coincide for small (where internal circulation is absent) and large (where surface tension forces cease to be important) bubbles (Clift et al., 1978).

For contaminated bubbles, Grace et al. (1976) (*apud* Clift et al., 1978) introduce the following correlation for *spherical* bubbles,

$$U_\infty = \frac{\mu_l}{\rho_l D_b} M_o^{-0.149} (J - 0.857), \tag{A.7}$$

where

$$J = \begin{cases} 0.94H^{0.757} & 2 < H \le 59.3, \\ 3.42H^{0.441} & 59.3 < H, \end{cases} \tag{A.8}$$

and

$$H = \frac{4}{3} E_o M_o^{-0.149} (\mu_l / 0.0009), \quad [\mu_l] = \mathrm{kg(ms)^{-1}}. \tag{A.9}$$

For non-spherical bubbles, the equivalent diameter (D_{eq}) must be used. D_{eq} is generally defined as the diameter of a spherical particle having the same volume of a considered bubble. For two dimensional particles, D_{eq} is the diameter of a circular particle having the same area of a considered bubble.

For D_{eq} > 1.3 mm, the top curve of Fig. A.23 can be approximated by

$$U_\infty = \left[(2.14\sigma / \rho_l D_{eq}) + 0.505\, gD_{eq} \right]^{1/2}. \tag{A.10}$$

For very large bubble volumes, the effects of surface tension and viscosity are negligible, the bubbles take on a spherical cap shape and the rise velocity is given by $U_\infty = (2/3)\sqrt{gR_l}$ (Davies and Taylor, 1950), where R_l is the radius of the upper surface of the lenticular body. Expressing this equation in terms of an equivalent radius (R_b), it follows immediately that

$$U^* = R^{*1/2}. \tag{A.11}$$

A2. The effects of flow confinement

When a single bubble rises in a confined environment, its velocity U_b is generally lower than that in extended liquids. An immediate parameter to account for velocity changes is the ratio between the bubble and pipe radii $\eta = R_b/R_p$. The results of Collins (1967) (*apud* Wallis (1969)) for large inviscid bubbles are

$$\eta < 0.125, \quad U_b = U_\infty, \tag{A.12}$$

$$0.125 < \eta < 0.6, \quad U_b = 1.13U_\infty e^{-\eta}, \tag{A.13}$$

$$0.6 < \eta, \quad U_b = 0.496U_\infty \eta^{-1/2}. \tag{A.14}$$

For *fluid* spheres, Edgar (1966) (*apud* Wallis (1969)) suggests

$$\eta < 0.6, \quad U_b = U_\infty(1 + 1.6\eta)^{-1}, \tag{A.15}$$

$$0.6 < \eta, \quad U_b = 0.12U_\infty \eta^{-2}. \tag{A.16}$$

By increasing gas flow rates, the large bubbles tend to bridge the pipe resulting in an elongated structure consisting of a near-spherical nose and a near-cylindrical finite body. Surrounding the bubble is a thin liquid film that flows downward. Since the pressure in the bubble is substantially constant, the pressure in the surrounding film must also be constant. This means that the gravity forces action on the film must be entirely balanced by the wall shear stress. Theory and experiments presented in Davies and Taylor (1950) for a large bubble confined inside a pipe suggest

$$U_b = 0.328\sqrt{gD_p}, \tag{A.17}$$

where D_p is the pipe diameter.

A3. The rise velocity of a single bubble in a flowing stream

The absolute rise velocity of a bubble in a flowing stream should simply be the vectorial composition of the local velocities of the liquid and of the bubble (Govier and Aziz (1977)), and this fact has been abundantly confirmed through experiments. For simple situations, where a bubble or a train of bubbles travel in a rectilinear trajectory, the local value of U_{bf} is thus

$$U_{bf} = U_L + U_{bs}, \tag{A.18}$$

with U_L = local liquid velocity, U_{bs} = bubble velocity in a stagnant fluid.

The difficulty in directly applying Eq. (A.18) to find the average, absolute velocity of bubbles in a flowing stream results from the uncertainties introduced by the nonuniform liquid velocity and bubble concentration across the pipe diameter. The analysis of Zuber and Findley (1965) has clarified that the average absolute velocity of a given phase may be expressed as the sum of a term proportional to the mixture velocity and the weighted average drift velocity, that is

$$U_{bf} = C_0 U_M + U_{bs}, \tag{A.19}$$

where C_0 is the flow distribution parameter, related to the velocity and concentration profiles and U_M = mixture velocity = $(Q_l + Q_g)/A$; A = cross sectional area of a pipe.

The value of C_0 is observed to lie between 1.0 and 1.5, with a preferred value of 1.2 (Wallis (1969)).

Nicklin et al. (1962) show that long bubbles of finite length in vertical tubes rise relative to the liquid ahead of them exactly with the velocity of wakeless bubbles of the type discussed in Davies and Taylor (1950). Nicklin et al. (1962) suggest

$$U_{bf} = 1.2U_M + 0.35\sqrt{gD_p}, \quad R_e > 8,000 \tag{A.20}$$

with D_p = pipe diameter.

A4. Formation and breakup of bubbles

It is only rarely that bubbles exposed to a turbulent flow attain a stable condition. Upon the action of eddies of various sizes, bubbles may be merely transported in the flow (*large* eddies) or made to deform and split up (*small* eddies). In fact, as bubbles are introduced in a flow, their size distribution is determined by the dynamics of coalescence and breakup. Without the addition of surface-active agents, bubbles tend to coalesce as they collide which one another. On the other hand, owing to the hydrodynamics forces provoked by the flow around them, bubbles may deform and breakup. Depending on the flow conditions, an equilibrium between these two processes may then eventually result in local stable conditions.

Bubbles can be formed in many ways. A typical manner of controlling the sizes of generated bubbles is the use of orifices with a known opening. Unfortunately, this process depends on the details of the orifice, the liquid and gas properties and flow rates in a very intricate fashion. For conditions in which the gas flow rate through an orifice is nearly constant, the size of generated bubbles can be predicted in terms of the time for which the bubble remains attached to the orifice as a result of buoyancy and surface tension effects. For moderate and large gas velocities, algebraic expressions can be obtained for bubble diameter predictions (Wallis (1969)). For gas velocities high enough so that bubbles are formed through the breakup of a jet, the observed radius is about twice the radius of the orifice. In industrial applications, however, bubbles are normally formed by a group of orifices or a porous wall and are exposed to so many disturbances due to the presence of singularity in transportation lines (elbows, tees, valves) that any predictive theory for the size of bubbles in a given position is only useful as a first approximation. It must then be clear that the size of bubbles and of any dependent variables such as void fraction, is then a function of not only the way in which bubbles are produced but also of the distance which they travel from the point of injection. Bubbles also change through significant pressure differences, expanding or collapsing.

The breakup of bubbles is generally (Hinze (1955)) described by way of three basic types of deformation: lenticular, cigar-shaped and bulgy deformations. Various flow patterns may cause a bubble to deform in any of the three basic deformations. Fundamentally shear stresses and irregular pressure fluctuations (as in a turbulent flow field) provoke bubble breakup.

According to Hinze (1955), in turbulent flows bubbles split primarily due to the action of eddies of comparable size and thus due to the dynamic pressure forces of the turbulent motion ($= \rho_l \overline{u^2}$, where $\overline{u^2}$ is the average squares of velocity fluctuations over a distance equivalent to the average size of the considered bubble).

Considering the previous discussion on dimensionless groups, the greater the value of W_e, the greater the effects provoked by external pressure over the interfacial-tension force. Provided the turbulent fluctuations are considered the responsible for bubble breakup, one may write

$$W_{e_{crit}} = \frac{\rho_l \overline{u^2} D_{b_{max}}}{\sigma}, \tag{A.21}$$

where $D_{b_{\max}}$ is the maximum size a bubble can sustain in the turbulent field defined by $\overline{u^2}$.

In Equation (A.21), Hinze (1955) suggests $W_{e_{crit}}$ = constant $\approx$ 1.18. The notion that there exists a critical value of W_e above which bubbles breakup is central to predictive models.

To correlate $\overline{u^2}$ and $D_{b_{\max}}$ the usual approximation is to consider the flow homogeneous and isotropic (Hinze (1955)). The implication is that the smallest eddies can be characterized through

Kolmogorov's scales for velocity and length so that

$$\overline{u^2} = C_1(\epsilon D_b)^{2/3}, \tag{A.22}$$

where $C_1 = 2$ and ϵ denotes the energy input per unit mass and unit time.

Combining Eqs. (A.21–A.22), it follows immediately

$$D_{b_{max}} = C_2\left(\frac{\sigma}{\rho_l}\right)^{3/5}\epsilon^{-2/5}, \tag{A.23}$$

with $C_2 = 0.725$ (Hinze, 1955).

Alternatively, consider $\overline{u^2} = (2/3)K$, where K is the turbulent kinetic energy per mass unit. The immediate result is

$$D_{b_{max}} = \frac{3}{2}W_{e_{crit}}\frac{\sigma}{\rho_l K}. \tag{A.24}$$

The $W_{e_{crit}}$ proposed by Hinze was based on one experimental data set, with 11 entries obtained for a liquid-liquid emulsion. Subsequent works criticized Hinze's analysis and offered alternative values for the critical Weber number. For liquid-liquid dispersions and conditions not very far apart from those discussed in Hinze, Narsimhan et al. (1979) suggest $W_{e_{crit}} = 0.256$. For air bubbles in water, Prince and Blanch (1990) used $W_{e_{crit}} = 2.3$.

Slight different propositions are further presented in literature. For gas-liquid bioreactors, Walter and Blanch (1986) introduce

$$W_{e_{crit}} = 1.12(\mu_l/\mu_g)^{0.1}. \tag{A.25}$$

For pipe flow, Hesketh et al. (1987, 1991) propose

$$D_{b_{max}} = 1.36W_{e_{crit}}^{0.6}\left(\frac{\sigma^{0.6}}{\rho_l^{0.3}\rho_g^{0.2}\mu_l^{0.1}}\right)\frac{D_p^{0.5}}{U_{sl}^{1.1}}, \tag{A.26}$$

where $W_{e_{crit}} = 1.1$, D_p is the pipe diameter and U_{sl} is the superficial liquid velocity.

Supplementary material

Supplementary material associated with this article can be found, in the online version, at doi:10.1016/j.ijmultiphaseflow.2020.103548

References

Ahmed, W.H., Ching, C.Y., Shoukri, M., 2007. Pressure recovery of two-phase flow across sudden expansions. Int. J. Multiphase Flow 33, 575–594.

Ahmed, W.H., Ching, C.Y., Shoukri, M., 2008. Development of two-phase flow downstream of a horizontal sudden expansion. Int. J. Heat and Fluid Flow 29, 194–206.

Aloui, F., Doubliez, L., Legrand, J., Souhar, M., 1999. Bubbly flow in an axisymmetric sudden expansion: pressure drop, void fraction, wall shear stress, bubble velocities and sizes. Exp. Thermal and Fluid Sci. 19, 118–130.

Attou, A., Bolle, L., 1999. A model for pressure drop of gas-liquid bubbly flow through an orifice or an abrupt pipe contraction. Chem. Eng. Technol. 22, 589–599.

Azzopardi, B.J., Ijioma, A., Yang, S., Abdulkareem, L.A., Azzi, A., Abdulkadir, M., 2014. Persistence of frequency in gas-liquid flows across a change in pipe diameter or orientation. Int. J. Multiphase Flow 67, 22–31.

Bhaga, D., Weber, M.E., 1981. Bubbles in viscous liquids: shapes, wakes and velocities. J. Fluid Mech. 105, 61–85.

Clift, R., Grace, J. R., Weber, M. E., 1978. Bubbles, Drops and Particles. Academic Press, New York, p. 380.

Collins, R., 1967. The effect of a containing cylindrical boundary on the velocity of a large gas bubble in a liquid. J. Fluid Mech. 28, 97–112.

Davies, R.M., Taylor, G.I., 1950. The mechanics of large bubbles rising through extended liquids and through liquids in tubes. Proc. R. Soc. London. Series A 200, 375–390.

Edgar, Jr., C. B., 1966. AEC rept. no NYO-3114-. 14, 19–21.

Fagundes Netto, J.R., Gonçalves, G.F.N., Silva Freire, A.P., 2019. Statistical moments transport model for the prediction of slug flow properties. Int. J. Multiphase Flow 120, 103086.

Galinat, S., Masbernat, O., Guiraud, P., Dalmazzone, C., Noik, C., 2005. Drop breakup in turbulent pipe flow downstream of a restriction. Chem. Eng. Sci. 60, 6511–6528.

Gonçalves, G.F.N., Baungartner, R., Loureiro, J.B.R., Silva Freire, A.P., 2018. Slug flow models: feasible domain and sensitivity to input distributions. J. Petroleum Sci. Eng. 169, 705–724.

Govier, G.W., Aziz, K., 1977. The flow of complex mixtures in pipes. Robert E. Krieger Publishing Company, New York.

Grace, J.R., Wairegi, T., Nguyen, T.H., 1976. Shapes and velocities of single drops and bubbles moving freely through immiscible liquids. Transact. Inst. Chem. Eng. 54, 167.

Hesketh, R.P., Etchells, A.W., Russell, T.W.F., 1987. Bubble size in horizontal pipelines. AIChE J. 33, 663.

Hesketh, R.P., Etchells, A.W., Russell, T.W.F., 1991. Bubble breakage in pipeline flow. Chem. Eng. Sci. 46, 1–9.

Hessenkemper, H., Ziegenhein, T., 2018. Particle shadow velocimetry (PSV) in bubbly flows. Int. J. Multiphase Flow 106, 268–279.

Hinze, J.O., 1955. Fundamentals of the hydrodynamic mechanism of splitting in dispersion processes. AIChE J. 3, 289–295.

Lage, P.L.C., Esposito, R.O., 1999. Experimental determination of bubble size distributions in bubble columns: prediction of mean bubble diameter and gas hold up. Powder Technol. 101, 142–150.

Lasheras, J.C., Eastwood, C., Martinez-Bazan, C., Montanes, J.L., 2002. A review of statistical models for the breakup of an immiscible fluid immersed into a fully developed turbulent flow. Int. J. Multiphase Flow 28, 247–278.

Liao, Y., Lucas, D., 2009. A literature review of theoretical models for drop and bubble breakup in turbulent dispersions. Chem. Eng. Sci. 64, 3389–3406.

Liao, Y., Lucas, D., 2010. A literature review on mechanisms and models for the coalescence process of fluid particles. Chem. Eng. Sci. 65 (10), 2851–2864.

Magnaudet, J., Eames, I., 2000. The motion of high-reynolds number bubbles in inhomogeneous flows. Annu. Rev. Fluid Mech. 32, 659–708.

Matamoros, L.M.C., Loureiro, J.B.R., Silva Freire, A.P., 2014. Length-area-volume of long bubbles in horizontal slug flow. Int. J. Multiphase Flow 65, 24–30.

Narsimhan, G., Gupta, J.P., Ramkrishna, D., 1979. A model for transitional breakage probability of droplets in agitated lean liquid-liquid dispersions. Chem. Eng. Sci. 34, 257–265.

Nicklin, D.J., Wilkes, J.O., Davidson, J.F., 1962. Two-phase flow in vertical tubes. Trans. Inst. Chem. Eng 40, 61–68.

Nogueira, S., Sousa, R.G., Pinto, A.M.F.R., Riethmuller, M.L., Campos, J.B.L.M., 2003. Simultaneous PIV and pulsed shadow technique in slug flow: a solution for optical problems. Exp. Fluids 35, 598–609.

Prince, M.J., Blanch, H.W., 1990. Bubble coalescence and break-up in air-sparged bubble columns. AIChE J. 36, 1485–1499.

Rinne, A., Loth, R., 1996. Development of local two-phase flow parameters for vertical bubbly flow in a pipe with sudden expansion. Exp. Thermal and Fluid Sci. 13, 152–166.

Schmidt, J., Friedel, L., 1997. Two-phase pressure drop across sudden contraction in ducts areas. Int. J. Multiphase Flow 23, 283–299.

Shermer, L., Gulitski, A., Barnea, D., 2007. On the turbulent structure in the wake of taylor bubbles rising in vertical pipes. Physics of Fluids 19, 035108.

Taitel, Y., Bornea, D., Duckler, A.E., 1980. Modelling flow pattern transitions for steady upward gas-liquid flow in vertical tubes. AIChE J. 26, 345–354.

van Hout, R., Gulitski, A., Barnea, D., Shermer, L., 2002. Experimental investigation of the velocity field induced by a taylor bubble rising in stagnant water. Int. J. Multiphase Flow 28, 579–596.

Wallis, G.B., 1969. One-dimensional Two-phase Flow. McGraw-Hill, New York.

Wallis, G.B., 1974. The terminal speed of single drops or bubbles in an infinite medium. Int. J. Multiphase Flow 1, 491–511.

Walter, J.F., Blanch, H.W., 1986. Bubble break-up in gas-liquid bioreactors: break-up in turbulent flows. Chem. Eng. J. 32, B7–B17.

Ziegenhein, T., Lucas, D., 2016. On sampling bias in multiphase flows: particle image velocimetry in bubbly flows. Flow Meas. and Instrumentation 48, 36–41.

Zuber, N., Findley, J.A., 1965. Average volumetric concentration in two-phase flow systems. J. Heat Transfer Trans. ASME 87, 453–468.